OPEN ACCESS

University of BRISTOL

Cook, R. G., Calderon, D. E., Cooper, J. E., Lowenberg, M. H., & Neild, S. A. (2019). Industrially-inspired Gust Loads Analysis of Various Aspect Ratio Wings Featuring Geometric Nonlinearity. *Journal of Aircraft*, *57*(1). https://doi.org/10.2514/1.C035294

Peer reviewed version

Link to published version (if available):
10.2514/1.C035294

Link to publication record in Explore Bristol Research
PDF-document

This is the author accepted manuscript (AAM). The final published version (version of record) is available online via American Institute of Aeronautics and Astronautics at https://arc.aiaa.org/doi/full/10.2514/1.C035294 . Please refer to any applicable terms of use of the publisher.

University of Bristol - Explore Bristol Research
General rights

This document is made available in accordance with publisher policies. Please cite only the published version using the reference above. Full terms of use are available:
http://www.bristol.ac.uk/red/research-policy/pure/user-guides/ebr-terms/

Industrially-inspired Gust Loads Analysis of Various Aspect Ratio Wings Featuring Geometric Nonlinearity

Journal:	*Journal of Aircraft*
Manuscript ID	2018-10-C035294.R1
Manuscript Type:	Full Paper
Date Submitted by the Author:	05-Jul-2019
Complete List of Authors:	Cook, Robert; University of Bristol Department of Aerospace Engineering, Calderon, Dario; University of Bristol Department of Aerospace Engineering, Cooper, Jonathan; University of Bristol, Department of Aerospace Engineering Lowenberg, Mark; University of Bristol, Aerospace Engineering Neild, Simon; University of Bristol, Mechanical Engineering
Subject Index Category:	81000 Structural Modeling < 80000 STRUCTURAL MECHANICS AND MATERIALS, 30100 Aircraft Dynamics < 30000 GUIDANCE, CONTROL, AND DYNAMICS TECHNOLOGY, 00200 Aeroelasticity and Aeroservoelasticity < 00000 AIRCRAFT TECHNOLOGY, CONVENTIONAL, STOL/VTOL
Note: The following files were submitted by the author along with the article. You may review these files online, if you wish. Acceptance for publication will be based solely on the content of the article.	
Effect of Geometric Nonlinearity on Gust Loads Analyses of Various Aspect Ratios - Rev 1.zip	

SCHOLARONE™
Manuscripts

Industrially-inspired Gust Loads Analysis of Various Aspect Ratio Wings Featuring Geometric Nonlinearity

R. G. Cook*, D. E. Calderon†, J. E. Cooper‡, M. H. Lowenberg§ and S. A. Neild¶
Department of Aerospace Engineering, Queen's Building, University Walk, Bristol, BS8 1TR.

This paper considers the effect of geometric nonlinearity on gust load analyses of high aspect ratio commercial aircraft. Three variants of a conceptual aircraft, featuring wing aspect ratios of 10, 18 and 26, are sized using an industrially-inspired procedure to obtain realistic structures of existing and future designs. These aircraft are modelled in a nonlinear aeroelastic framework, featuring a geometrically-exact beam formulation coupled with unsteady aerodynamics, and subjected to a gust loads process adapted for nonlinear systems. The gust analysis is also carried out using a linear approach (linearising the equations of motion about an undeformed or trimmed geometry) to understand how nonlinearities influence the loads and dynamic behaviour of aircraft as the aspect ratio increases. Load envelopes show that vertical shear and bending moments are predicted well by the linear analyses, even for the aspect ratio 26 case, providing that the linearisation is performed about the trimmed geometry. In contrast, the in-plane and axial loads are significantly underestimated using linear analyses. Torque behaviour is problem specific, and therefore difficult to generalise. Even on the aspect ratio 10 case, which would traditionally be considered as a linear problem, it can shown that the torque loads are considerably affected by nonlinearity.

For Peer Review

Nomenclature

1MC	1-minus-cosine
a	Body-fixed Reference Frame
A	Local Aerodynamic Reference Frame
AR	Aspect Ratio
B	Local Structural Reference Frame
$[C]$	Sectional Compliance Matrix
$[C^{xy}]$	Rotation matrix mapping from a variable in the y frame to the x frame

*Research Associate
†Research Associate
‡Royal Academy of Engineering Airbus Sir George White Professor of Aerospace Engineering, FAIAA.
§Professor of Flight Mechanics, Department of Aerospace Engineering
¶Professor of Nonlinear Dynamics, Department of Aerospace Engineering

$\boldsymbol{F}$	Vector of Local Axial/Shear forces, $\{F_x\ F_y\ F_z\}^T$
F_x	Local Beam Axial force
F_y	Local Beam Fore-Aft Shear
F_z	Local Beam Vertical Shear
$\boldsymbol{f}$	Vector of Applied Forces
G	Global Reference Frame
g	Gust Reference Frame/Acceleration due to Gravity
$\boldsymbol{g}$	Acceleration due to Gravity
$\boldsymbol{\gamma}$	Vector of Local Strains
$\boldsymbol{H}$	Vector of Rotational Momenta
HAR(W)	High Aspect Ratio (Wing)
$\boldsymbol{\kappa}$	Vector of Local Curvatures
$\boldsymbol{M}$	Vector of Local Torsional/Bending Moments, $\{M_x\ M_y\ M_z\}^T$
M_x	Local Beam Torque
M_y	Local Beam Bending Moment
M_z	Local Beam Fore-Aft Moment
$\boldsymbol{m}$	Vector of Applied Moments
m	Sectional Mass per Unit Length
$[M]$	Sectional Mass Matrix
$\boldsymbol{\Omega}$	Local Rotational Velocities
$\boldsymbol{\omega}$	Body-Fixed Reference Frame Rotational Velocities
$\boldsymbol{P}$	Vector of Translational Momenta
$\boldsymbol{R}$	Position Vector from the origin of the body-fixed frame to the local beam frame
RTC	Round-the-Clock
s	1D curvilinear coordinate of a point along a deformed beam
$\boldsymbol{V}$	Local Translational Velocities
$\boldsymbol{v}$	Body-Fixed Reference Frame Translational Velocities
$\boldsymbol{x}$	Vector of Beam Velocity and Load States

For Peer Review

I. Introduction

High aspect ratio wings (HARW) can lead to significant drag savings due to the reduction in induced drag at operating design points, but can also suffer from increased bending moments; the resulting increase in structural weight from this can negate the fuel burn savings. Typically such designs have little or no sweep and therefore the beneficial gust alleviation due to bending-torsion coupling inherent in sweptback designs is absent (with some exceptions). HARW are also prone to nonlinear aeroelastic instabilities (as shown by the Helios crash[1]), and these nonlinear effects are usually not well understood; therefore the wing is often stiffened to avoid large deformations with the penalty of significant weight increases. Greater flexibility could also result in a strong coupling between structural dynamics and flight dynamics, as well as undesirable effects on the handling and ride qualities. A further limitation on larger span designs is the size restriction on airport gates and ground handling.

One particular aspect of aircraft design is understanding how exogenous forces and excitations on the aircraft affect the structural loads in order to demonstrate that the aircraft can withstand certain operating conditions. In an industrial setting, tens of thousands of simulations are often carried out, considering static manoeuvre, gust, landing and taxiing cases for combinations of multiple flight points and mass cases. In this paper, the impact of geometric nonlinearities on the results and processes of gust loads analysis is investigated.

(a) Airbus Concept Plane[2] (b) Boeing's Strut-Braced SUGAR Volt Concept[3]

Fig. 1 Future HARW Aircraft Concepts

A number of high aspect ratio wing configurations are being considered, and both Airbus and Boeing have published their own concepts, as shown in Figure 1. The Boeing SUGAR Volt aircraft[4] includes a strut to brace the wing, which will help reduce structural mass at the expense of additional drag. Other aspects such as the engine position, and type, need to be considered, as the engine could have a detrimental effect on the dynamics of a high aspect ratio wing. Technologies such as passive and active gust and manoeuvre load alleviation systems could also mitigate the effects of loads transferral from atmospheric disturbances into the structure.

The modelling of highly flexible structures has been quite thoroughly investigated (and discussed shortly) with

Review copy- Do not distribute

significant focus on unmanned aerial vehicle (UAV) designs. When extending analyses beyond the traditional aeroelastic approaches, straight-forward and robust model reduction techniques, as favoured in industry[5], can no longer be used. Approaches such as modal decomposition and frequency-based aerodynamics (e.g. doublet-lattice method) are no longer valid in the nonlinear regime, so efforts in the literature are often focussed on avoiding excessive computation when considering time-marching solutions to nonlinear systems. Structural aspects of a highly flexible aircraft are typically represented using a beam, or set of interconnected beams, which is a valid assumption to make on a slender structure with negligible chord-wise bending. Various approaches in the literature consider displacement-based[6, 7], strain-based[8–10], and intrinsic-based[11] approaches to the nonlinear beam modelling problem. Generally, aerodynamics have also been modelled with lower-order models based on incompressible, inviscid, low speed assumptions. While the commonly used doublet-lattice method (DLM) can be cast into the time-domain through the use of rational function[12] or minimum-state approximations[13] in cases where the flow is assumed to be linear and other sources of nonlinearities are not due to large deformations (control surface free-play as one example), the validity of this approach is questionable in HARW applications. As such, strip-theory has often been favoured for the significant computational benefits[14, 15], where a number of unsteady methods have been presented[16, 17], including models with the ability to predict viscous effects like stall[18, 19]. However, it has been shown that 3D effects can become important[20], even for HARW applications[21], and so unsteady vortex-lattice method (UVLM) based approaches are becoming more frequently used, with the added 3D and wake effects that can be captured[22, 23] while still assuming inviscid and incompressible flow. While higher-order structural and aerodynamic methods are sometimes used[24], the computational expense currently limits the application to individual cases of interest rather than large numbers of computations over the whole envelope. Despite the development of aerodynamic reduced order models (ROMs)[25] and corrections to established methods[26, 27], the work in this paper is focused on the industrial implications of structural nonlinearities, and as such, a strip theory approach coupled with a nonlinear beam solver is deemed to be sufficient to capture important phenomena without modelling extraneous details.

One aspect of nonlinear aeroelastic modelling which is not often addressed in the literature is the impact that these nonlinearities have on aircraft design, and in particular when applied to commercial, passenger or freight aircraft. In one recent paper, Calderon *et al.* [28] use nonlinear aeroelastic models in an industrial sizing routine to understand how nonlinear effects change the design versus a linear model, but noting that the load cases included in this analysis were all static due to the computational limitations of carrying out nonlinear dynamic simulations in an optimisation routine. In contrast and despite their shortcomings for modelling nonlinearities, established linear methods can handle such large numbers of simulations required of an industrial process in a robust, reliable and efficient fashion. As such, aspects of these techniques are still going to be retained in the industrial analysis of next-generation aircraft. Understanding how linear and nonlinear results differ for a particular class of aircraft can potentially give aerospace designers guidelines for interpreting linear results in such a way as to factor in nonlinearities (if, indeed, broad and general rules can be

For Peer Review

observed). Furthermore, if certain system states are shown to behave in a largely linear way, then it could suggest areas of future work where nonlinear equations can be partially linearised with respect to those degrees of freedom. A similar idea is presented by Hesse[7], who outlines an approach to linearising nonlinear equations with respect to structural deformations, while still retaining the nonlinear rigid-body equations allowing for arbitrarily large aircraft rotations and correct modelling of centrifugal forces, and Coriolis and Euler damping terms.

In this work, the effect of increasing aspect ratio on aircraft gust loads is investigated, which is widely regarded as leading to more significant geometric nonlinearity (when tip displacements exceed 10-20% span as a general rule of thumb). To do this, a series of commercial aircraft with different aspect ratios are sized using an in-house sizing tool[29] inspired by industrial processes. With aspect ratios of 10, 18 and 26, the three resulting aircraft structures are representative of both current and future passenger aircraft designs, with realistic internal structures consisting of box sections with optimised thickness properties to ensure minimum mass without exceeding maximum stress. These aircraft are then modelled using a nonlinear aeroelastic solver, featuring geometrically-exact structural modelling and unsteady aerodynamics, on the assumption that large deformations are likely to occur in-flight. A gust loads process is developed for nonlinear systems, which is capable of carrying out the type of gust excitations required by regulatory bodies. In particular, lateral and round-the-clock (RTC) gusts are required for certification loads (in addition to longitudinal gusts), meaning that certain orientations of gust excitation may become more important in the gust loads analysis for highly-flexible aircraft. This study considers how changes in aspect ratio, towards future designs, affect the gust loads on the structure, considering when the inclusion of geometric nonlinearity in the analysis becomes important. It should be noted that the nonlinearities studied in this work would also affect flight dynamics behaviour, which would in turn have an effect on things such as handling and ride quality - however, the focus of this paper is solely on the loads due to its importance for structural integrity.

Initially in §II, the nonlinear aeroelastic approach used in this work, along with gust input definitions, is presented. After this, the specific aircraft models are described in §III, followed by a discussion of 1g and dynamic gust loads analyses results in §IV. Finally, conclusions on worst-case gust loads and linear versus nonlinear analyses are drawn in §V.

II. Aeroelastic Modelling

The methods used for modelling aeroelastic systems with nonlinear effects are briefly described in this section. A definition of reference frames used in this study is detailed. Then the structural model is presented, followed by the aerodynamics. Finally, the implementation of the equations is introduced.

For Peer Review

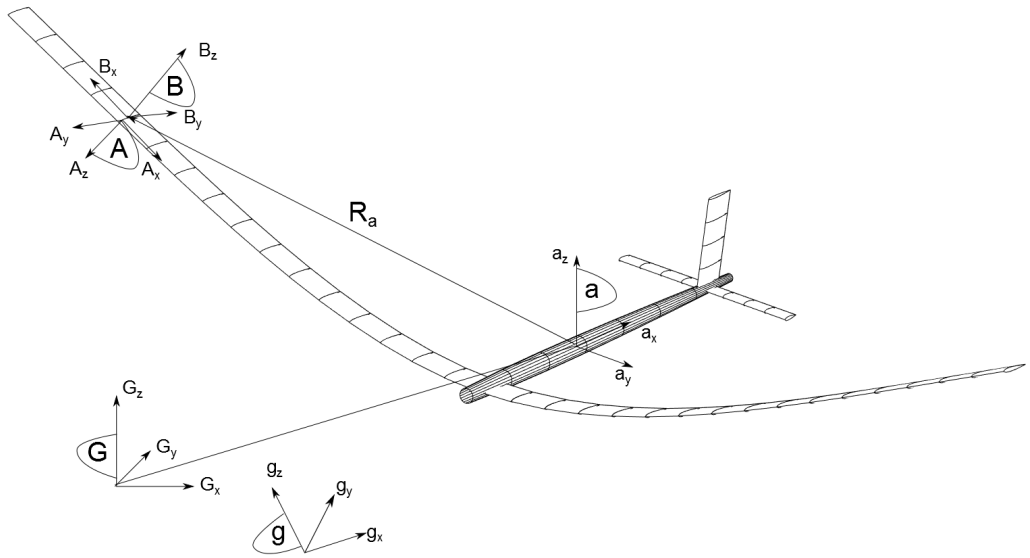

Fig. 2 Reference frames used in the aeroelastic model formulation.

Peer Review

A. Reference Frame Definitions

A number of reference frames need to be defined to clarify in which frame certain variables relating to the structural and aerodynamics are expressed. Figure 2 illustrates a generic, highly flexible aircraft structure, and labels the reference frames. The wings, fuselage and tailplane can all be modelled as beams.

The *global reference frame*, G, is an earth-fixed inertial reference frame (assuming a flat and non-rotating earth). The effect of gravity is expressed in this frame as a vector in the z-axis, $\boldsymbol{g}_G = [0; 0; -g]$, where g is the acceleration due to gravity. The *body-fixed reference frame*, a, is a reference frame that is free to move in translation and rotation within the global reference frame. It is, as its name suggests, rigidly fixed to a point on the aircraft, with deformations of the structure defined relative to the body-fixed frame. For convenience, the origin of the body-fixed frame is chosen to be a point on the fuselage, with the x-axis aligned in the nose-to-tail direction. The centre of gravity of the system will move independently of this frame. The *local reference frame*, B, is a reference frame that is rigidly connected to the set of beams representing the structure (wings, fuselage, tail, etc.). All loads are given in this reference frame. The x-axis of the local reference frame B is parallel to the undeformed beam (assuming no pre-strains). The *aerodynamic reference frame*, A, is a reference frame that is rigidly connected to the beam, with the origin located at the aerodynamic centre of the aerofoil section at that beam location. It is convenient to define a separate reference frame for the aerodynamics to account for any rotations, such as twist or dihedral, that would mean that the aerodynamic reference frame was no longer coincidental with the local reference frame, B. The *gust reference frame*, g, is introduced to simplify the gust description. It is a frame that can have an orientation and position independent of the global reference frame, G. In the

Review copy- Do not distribute

gust reference frame, all gust velocities will be given as a purely vertical velocity vector. The gust reference frame can then be oriented in the global reference frame as required to produce a family of gusts.

B. Structural Modelling - Intrinsic Beam Formulation

The structural method used in this work is an intrinsic beam approach, as presented by Hodges[11]. While this approach is well documented and widely used in the literature, a brief description of the specific method of solving the intrinsic beam equations in this paper is included in Appendix .A to understand the particular application of the nonlinear beam formulation that will be used in the following work.

As part of on-going validation of nonlinear codes at the University of Bristol, this particular implementation has been compared in terms of accuracy and computation times with a number of alternative nonlinear beam formulations. Previous comparisons and summaries of all the beam models for static aeroelastic analyses was made in Howcroft *et al*.[30] showing a good agreement between the different methods.

C. Aerodynamics

To apply representative aerodynamic forces to the structural model, an unsteady strip theory is used. Strip theory has been shown in the literature to provide a reasonable approximation to aerodynamic forces for HARW, but lacks the induced drag terms and 3-dimensional effects that panel methods such as the DLM, VLM and UVLM can provide. Notwithstanding, the computational speed of strip theory allows for rapid assessment of numerous aeroelastic cases, and gives a useful, first-case insight into aeroelastic phenomena. The computational efficiency of this method is particularly important in this paper considering the hundreds of simulations required for each aircraft to thoroughly interrogate the space of regulation gust excitations.

An important point to note is that transonic and stall effects are not included in these analyses in order to study the effect of nonlinearities due to large deformations of the structure only. The airfoil sections rotate in a geometrically-exact manner, as defined by the structure, such that the lift vector is applied to the aircraft model correctly but the relationship between the angle-of-attack and the lift is linear.

Unsteady effects are included into the strip theory approach used here via Leishman's indicial response method[17] (using Jones' approximation to Theodorsen's function[31]). Palacios *et al*.[21] showed how Leishman's two-state approach was comparable in terms of accuracy to other methods such as Peters' Finite-State approach [16] requiring 4-8 states, with the obvious benefit of a vastly reduced number of aerodynamic states. The aerodynamic forces and moments are determined from the local beam velocities and local velocity fields due to gust disturbances, and enter into the structural equation, Eq. 7. Static lift slopes are calculated from an incompressible VLM solver to provide 3D tip loss effects, and are included into the strip-theory approach by updating the lift-curve slope.

For Peer Review

D. Numerical Implementation

The equations of motion are solved in MATLAB. The static solver uses a Newton-Raphson method to solve the FE discretisation of Eq. (7) with time derivatives set to zero, for an arbitrarily defined flow condition, aircraft orientation and control surface deflection. The total number of states for the static system for the formulation used in this work is therefore $6n$, where n is the number of elements of the system. A trim solver is written in MATLAB, which also uses a Newton-Raphson method to determine the orientation and control surface deflections (only angle of attack and elevator deflections are required) in order to balance the forces and allow for straight, level flight. As there is no drag included in this analysis, thrust is not required in the trimming routine for this aerodynamics model.

The dynamic solver solves Eq. (12) simultaneously with Eq. (14), along with the velocity integration equations in Eqs. (17) and the unsteady aerodynamic equations, using a Newmark-β time-stepping solver, similar to the implementation used in Shearer and Cesnik[32]. The total state size of the free-flying beam system is $12n + 6$, with an additional $7n$ states for temporal velocity integration to obtain positions and orientations, and a further $2n$ states for the unsteady aerodynamics states, resulting in a total of $21n + 6$ states.

In addition to the full nonlinear simulations, the equations are fully linearised and solved in MATLAB's in-built linear solver, *lsim*. This approach is useful for two main reasons. Primarily, it provides a solution representative of standard linear approaches used in a traditional gust loads approach, thus highlighting the situations where modelling the nonlinearities is important. It additionally allows for a rapid, first-case solution of the gust loads process, particularly when linear model reduction techniques are used, allowing for a better understanding of the worst case gusts before the more costly nonlinear simulations are run, and therefore means the gust excitation parameters can be narrowed down. This approach is discussed in more detail in §II.E. Furthermore, two different linearisations of the equations are carried out in this paper. First, the equations will be linearised about the undeformed geometry, which is representative of the traditional, linear approaches in industry, and particularly the method that is carried out in the industry standard software MSC.NASTRAN. The second linearisation will be carried out around the trimmed geometry. This more accurate approach identifies whether the differences that are seen between traditional linear and nonlinear aeroelastic simulations are fundamentally due to the linear assumption, or simply due to linearisation about a less representative static (undeformed) geometry.

E. Gust Loads Process

A gust loads process will be carried out which largely follows the FAA[33]/EASA[34] gust regulations for discrete atmospheric events, representing the gust disturbance as a 1-minus-cosine (1MC) excitation. If the trimmed aircraft flies with a velocity component purely in the x-direction of the global reference frame, G, and the x-axis of the gust reference frame, g, is parallel with this vector also, then the gust velocity, $\boldsymbol{w}$, in the gust reference frame is $\boldsymbol{w}_g = \left[\begin{array}{ccc} 0 & 0 & \frac{1}{2} w_{g_{max}} (1-\cos(\frac{\pi x}{H})) \end{array}\right]^T$, where x is the distance into the gust, H is the gust gradient, and $w_{g_{max}}$ is the gust

Review copy- Do not distribute

velocity amplitude as determined the regulations. A round-the-clock (RTC) gust can be constructed by rotating the gust reference frame around the x-axis of the global reference frame such that,

$$\boldsymbol{w_G} = \left[C^{Gg}\right] \boldsymbol{w_g} \quad \text{where} \quad \left[C^{Gg}\right] = \begin{bmatrix} 1 & 0 & 0 \\ 0 & \cos(\theta) & \sin(\theta) \\ 0 & -\sin(\theta) & \cos(\theta) \end{bmatrix}, \tag{1}$$

where if $\theta = 0°$, the gust is purely vertical, and if $\theta = 90°$ the gust is purely lateral. At any given moment in time, the positions of the lifting surfaces can be located with respect to the gust velocity field; these velocities are added to the local velocities of the lifting surfaces to include the gust excitation into the formulation.

Due to the nonlinearities that are introduced through the geometrically exact formulation in the structural equations, the typical industrial approach used on linear systems must be adapted. In a standard industrial gust loads process on a linear aeroelastic system, the 1g loads at the trim condition and the additional incremental gust loads can be calculated separately and added together in post-processing due to the linear approximations of the model[5]. Furthermore for a linear system, only vertical and lateral gusts need to be calculated, with negative and RTC gusts also determined in post-processing, again due to superposition assumptions that are only valid for linear systems. RTC gusts are usually only considered in cases where the loads on a particular component are comparable in magnitude when experiencing vertical or lateral gust excitations, for example a T-tail configuration or a wing featuring an engine. In a HARW, it may be the case that a highly deflected wing can make the structural loads due to both vertical and lateral excitations similar enough in magnitude that RTC gusts could become necessary, i.e., the worst case gust may not be a perfectly vertical or lateral gust, but at some angle. However, because of the nonlinearities associated with HARW, the aforementioned linear approach can no longer be applied here.

While RTC loads can be determined quickly in a linear system, there is no way to determine this for a nonlinear system without simply running combinations of gust orientation, θ, in an attempt to capture the worst case gusts. When considering the 'sufficient number' of gust gradients, H, required in the certifications, it implies that an excessively large number of simulations is required to thoroughly explore the problem space in a nonlinear aeroelastic system. Previous studies[35] showed how, even for exceptionally large structural deformations, the RTC gust cases could be identified reasonably accurately using a linearisation of the system equations providing that it is performed about the trim, rather than the undeformed geometry. Further developments of that work showed how a surrogate model based on the linear system of an aircraft alone could identify atypical gusts that exceeded the gust envelope that would have been determined from vertical and lateral gusts alone[36]. A simplified approach to that used in Cook *et al.*[36] is used here, whereby a gust analysis is first carried out on the linear system and the worst case gusts are identified for all loads directions across all beam elements of the FE problem before considering the nonlinear behaviour (the aircraft in Ref.

Review copy- Do not distribute

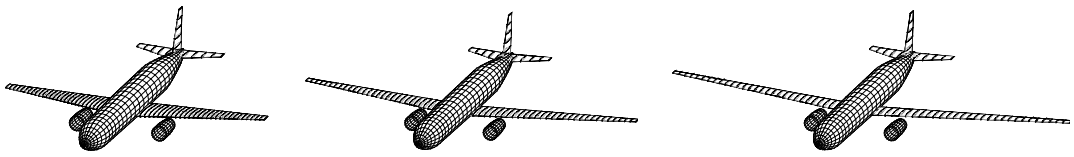

(a) AR 10 (b) AR 18 (c) AR 26

Fig. 3 The different aspect ratios studied in this work.

[36] is the same as used in this study).

For the gust loads analysis, 1MC gusts with lengths, $2H$, from 20m to 220m in 20m increments are considered (roughly the range required by the regulations[33, 34]). These gust excitations are input as disturbances on the linearised undeformed geometry first, without gravity or any angle of attack included in the linearisation. The aircraft is then trimmed using a static nonlinear solver, finding the angle of attack and elevator deflections to balance forces and moments. Using this trimmed state, simulations considering the same gust excitations are repeated on the linear system linearised about the trim condition. Finally, the full nonlinear simulations are carried out. Starting from the trimmed geometry, the aircraft is disturbed by the same gust lengths as in the linear analyses, in addition to those same gust lengths rotated about the flight axis by angles, θ, between 0° to 180° in 30° increments. The worst case gust lengths and RTC gust angles are also collated from the linear analysis and added to the previously defined set of gust excitations. Such an approach is not guaranteed to find the worst case gust excitations for the nonlinear system, but should at least capture cases that exceed the traditional envelope without the necessity of running large numbers of simulations.

III. Aircraft Model

In this work a range of conceptual commercial passenger aircraft with different aspect ratio wings are considered; an aspect ratio 10 aircraft is included as a representation of past and current designs, roughly equivalent to an Airbus A320-series aircraft; a variant with an aspect ratio of 18 is considered to represent potential, near-future planforms, similar to Boeing's SUGAR Volt for example (without the strut); and finally, an exaggerated aspect ratio 26 planform is considered to accentuate the geometric nonlinearities that may be seen, and to explore extreme ends of the design space. It should be noted that, in the context of this paper, the aspect ratio 10 case may often be referred to as 'low aspect ratio' relative to the aspect ratio 18 and 26 wings in the forthcoming results and discussion sections, despite being reasonably high in the general aerospace sense. Renderings of the aircraft that are being modelled in this work are shown in Fig. 3.

The overall geometry of the three aircraft planforms is influenced by data found in the literature on similar types of aircraft, and the internal structure of the wings, horizontal tail plane (HTP) and vertical tail plane (VTP) are represented as box sections that fit within the selected geometry. The box section properties are condensed into a beam representation,

Review copy- Do not distribute

Aspect Ratio (-)	10	18	26
MTOW (kg)	71000	75600	82000
Half Wing Mass (kg)	7360	9630	12900
Half HTP Mass (kg)	706	706	706
VTP Mass (kg)	578	578	578
Wing Half Span (m)	18.3	24.6	29.6
Breguet Range (km)	5930	6670	6780
Trim AoA (°)	6.4	6.7	7.9
Trim Elevator (°)	4.0	8.3	12.6

Table 1 Properties of the aircraft variants used in this work.

and various static trim and manoeuvre cases are applied to the structure to determine the maximum stresses in operation. The sizing routine determines the appropriate skin, spar and stringer thicknesses for the wingbox sections (assuming a fixed thickness to chord ratio, and only applied to the wing structure) by using MATLAB's in-built *fmincon* function to minimise mass while not exceeding the stress allowables of the material. A much more in-depth discussion of the process can be found in Calderon *et al.*[28, 29].

The aircraft is sized at various flight and mass cases within the flight envelope, including the cruise case at Mach 0.7 at an altitude of 10,000m and at the maximum take-off weight (MTOW). All future analyses are also run at this cruise condition. The wing is made of aluminium, with a Young's modulus of 69.9GPa, Poisson's ratio of 0.33, and a density of 2700kgm^{-3}. No structural damping is assumed. The wing is sized with engines on the wing at a fixed distance from the fuselage for all aspect ratios. The engines and pylons are assumed to be rigid, and have no aerodynamic contributions. Furthermore, because there is no drag assumed in the aerodynamics model, the engines do not apply a thrust. It was found in initial studies for this paper that a viscous drag term in the aerodynamics affects the 1g loads but the incremental gust loads were not affected significantly, and so, including viscous drag had little effect on the qualitative results.

The quarter-chord wing sweep and area are 12° and 130m^2, respectively, with a taper ratio of 0.25, fixed for all aspect ratios. Table 1 gives the resulting properties of the sized wing considering the three aspect ratios used in this work (the Breguet Range and trim condition calculations include the effects due to deformation of the wings). The angles of attack and elevator deflections in Table 1 are slightly higher than would be seen in practice due to a lack of pre-twist, wing setting angle or camber on the wing sections, and the incompressible flow assumptions resulting in lower lift-curve slopes. This is deemed to be a reasonable assumption to make for an initial design loop study, as in this work.

Table 1 shows that the total mass of the aircraft increases with aspect ratio, but despite this, the performance (in this case quantified using Breguet range) increases with aspect ratio. The optimum aspect ratio for maximum Breguet range falls somewhere between the 18 and 26 models[29], given the specific assumptions and constraints applied in this work. The MTOW is allowed to increase with aspect ratio to ensure that the fuel capacity and payload remain constant, and the capabilities of the different aspect ratios are consistent.

Review copy- Do not distribute
For Peer Review

IV. Gust Loads Analysis

Results of the gust loads process are presented next. To begin, a nonlinear trim solution is carried out, and eigenvalue analyses are performed on the different aspect ratio aircraft to determine the underlying modal behaviour. After this, the results of the gust loads process are presented and summarised.

A. Displacements

The 1g trim deflections are plotted in Fig. 4 comparing the trim shape for the three different aspect ratios. In addition, the maximum and minimum deflection envelopes from the gust loads process are shown (this is discussed later). The trim angle and elevator deflections are given in Tab. 1. It can be seen how, as the aspect ratio increases, the tip deflection, as a percentage of span, also increases. The static trim tip deflections for the aspect ratio 10 case are just below 4% of the semi-span, and the maximum deflection for all gusts is just above 6%, indicating it is likely to be operating in the linear regime. As the aspect ratio increases to 18 and 26, the maximum gust deflections increase to approximately 15% and 20%, respectively, of the span which indicates that nonlinear effects may become important[30]. It should be noted however, that the deformations are not exceptionally large, even for the aspect ratio 26 case (compared to UAV wings like those studied by Patil *et al.*[14] for instance). The tip-shortening effects due to the geometrically-exact formulation can be seen, particularly as the aspect ratio increases to 18 and 26.

Similar plots can be found in Fig. 5, illustrating the 1g angle of attack distributions down the wing, with the maximum and minimum angles of attack due to gust excitations. It can be seen that as the aspect ratio increases the root angle of attack increases (as also noted in table 1), but there is also a reduction in angle of attack along the span. From the angles of attack in Fig. 5 it would be possible that stall effects could become apparent here, though such effects are not captured by the aerodynamics model.

B. Stability Analysis

Stability analysis is carried out on the aircraft using an eigenvalue analysis of the linear system matrix. A root locus diagram is shown in Fig. 6 for aspect ratios 10, 18 and 26 for various aeroelastic modes of interest, comparing linearisations about the undeformed and trimmed geometries.

In Fig. 6 the imaginary parts of the flexible modes can be seen decreasing with increasing AR, which indicates a reduction in frequency which would be expected from such an increase in aspect ratio. The real parts also tend to decrease on these flexible modes as aspect ratio increases, showing a tendency for increased damping in these modes, although this damping reduces again as the aircraft reaches aspect ratio 26, for example in the first bending modes. The rigid body modes show a tendency to increase in both real and imaginary part, implying the rigid body modes increase in frequency slightly as aspect ratio increases, while the damping of these modes decreases.

It can also be seen in Fig. 6 that the real and imaginary parts of the eigenvalues associated with the first and

For Peer Review

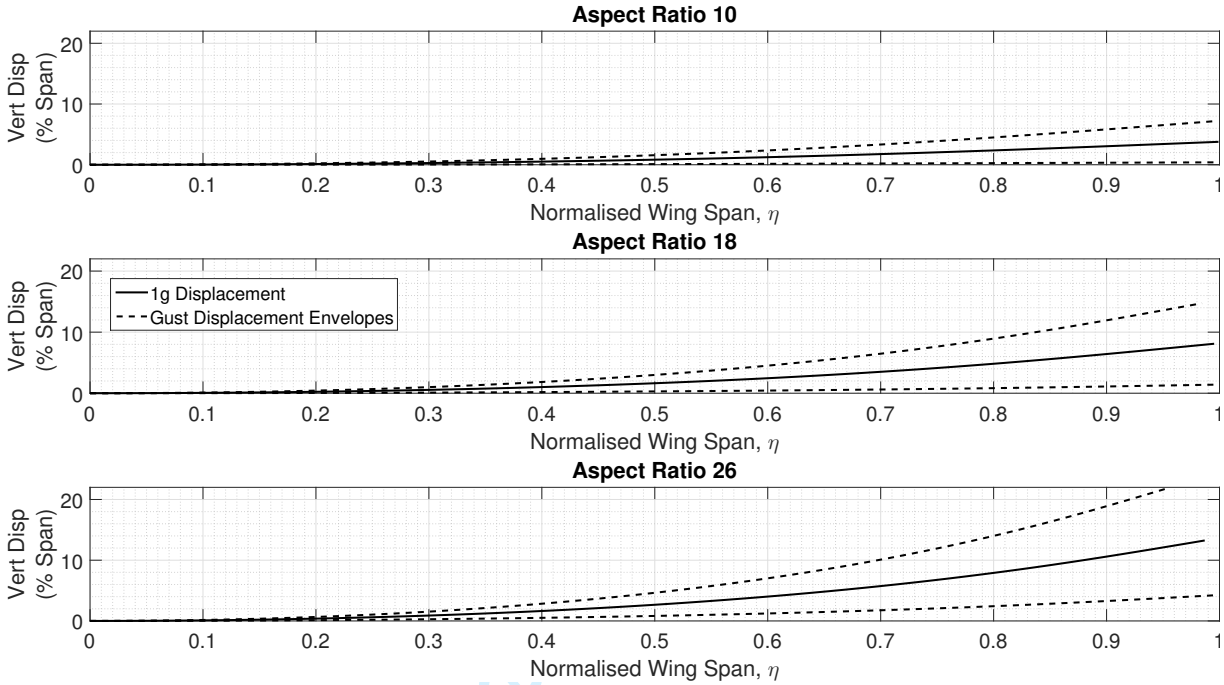

Fig. 4 Vertical displacement as percentage span vs. non-dimensionalised span for 1g deformations and maximum and minimum deformations from the gust loads analysis.

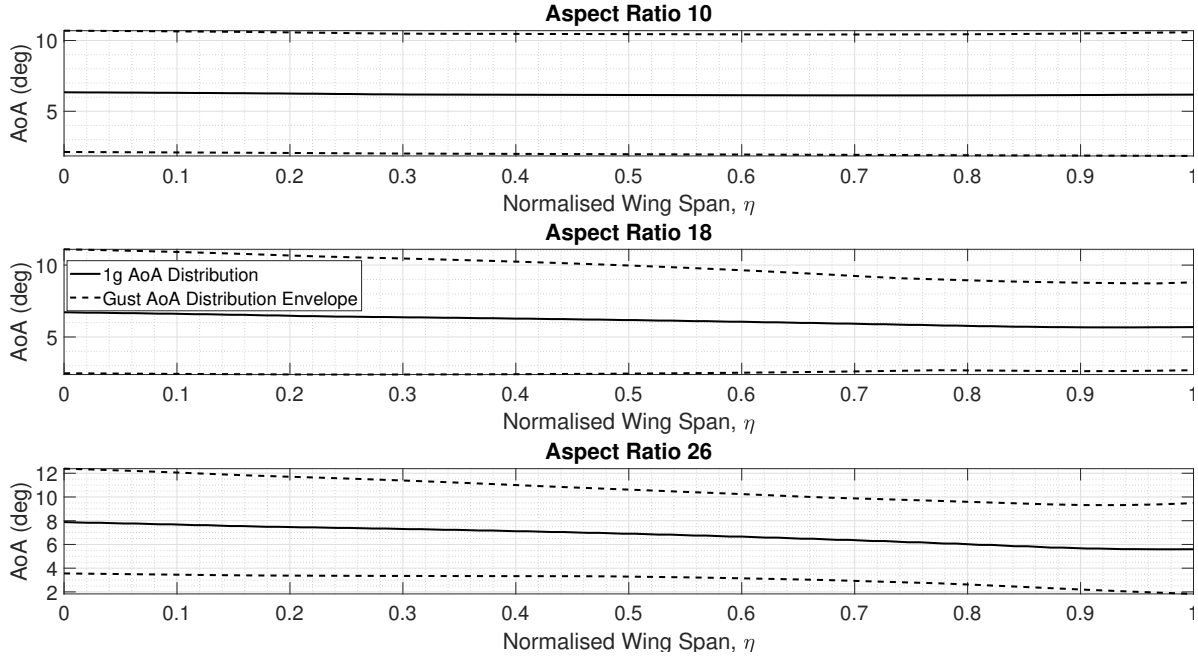

Fig. 5 Angle of attack distributions vs. non-dimensionalised span for 1g deformations and maximum and minimum angle of attack distributions from the gust loads analysis.

Review copy- Do not distribute

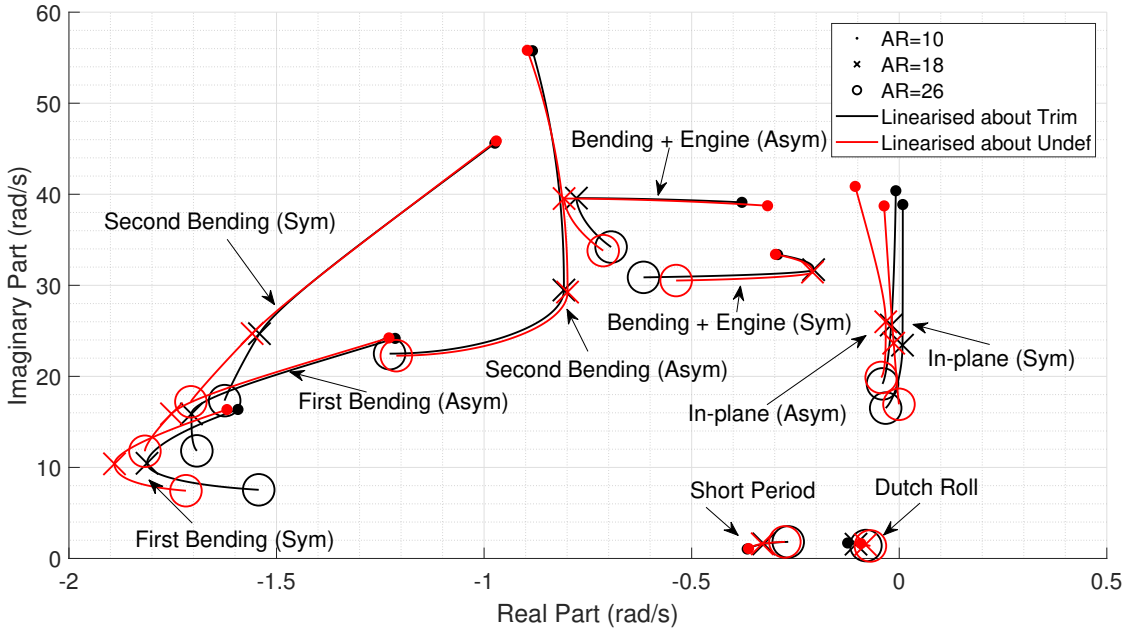

Fig. 6 Eigenvalue/pole root loci for various aspect ratio wings.

	AR 10		AR 18		AR 26	
	Undeformed (Hz)	Deformed (Hz)	Undeformed (Hz)	Deformed (Hz)	Undeformed (Hz)	Deformed (Hz)
Short Period	0.18	0.18	0.26	0.26	0.29	0.29
Dutch Roll	0.26	0.27	0.24	0.25	0.22	0.22
First Bending (Sym)	2.62	2.62	1.68	1.69	1.22	1.22
First Bending (Asym)	3.86	3.85	2.54	2.54	1.90	1.90
In-plane (Sym)	6.16	6.19	3.76	3.73	2.70	2.63
In-plane (Asym)	6.50	6.43	4.14	4.08	3.16	3.05
Second Bending (Sym)	7.30	7.26	3.94	3.94	2.75	2.77
Second Bending (Asym)	8.88	8.88	4.66	4.69	3.55	3.59
Bending + Engine (Sym)	5.32	5.31	5.01	5.05	4.86	4.92
Bending + Engine (Asym)	6.17	6.23	6.29	6.30	5.38	5.44

Table 2 Comparison of deformed vs. undeformed mode frequencies for different aspect ratios.

Review copy- Do not distribute

second bending modes (both symmetric and asymmetric) match well between the linearised-about-undeformed and linearised-about-trim geometry for the aspect ratio 10 case. However, as the aspect ratio increases, the differences also increase. Conversely, certain modes such as in-plane bending modes and bending-plus-engine modes display different real and imaginary parts between the different linearisation approaches even from the aspect ratio 10 case, which indicates that linearising about the trimmed geometry can affect the damping and frequency of the linear system even for low AR wings. The symmetric and asymmetric in-plane bending modes, for example, exhibit quite lightly damped behaviour in the undeformed case for any aspect ratio. However, once the trimmed geometry is included in the linearisation, the damping changes, reducing significantly for the low AR wing (and becoming marginally unstable) and increasing for the highest AR case.

Also observe in Fig. 6 that the bending-plus-engine mode (essentially a torsional mode) interacts to different degrees with the asymmetric second bending mode. As the engine span-wise location is fixed for all aspect ratios, there is little interaction of the engine with the bending modes for the low aspect ratio case, but at the aspect ratio 18 case, the root loci come together, and then part again as the aspect ratio is increased further. Without the engines, the asymmetric second bending mode root locus trajectory follows the path of the symmetric second bending mode root locus. The frequency of oscillation for the different modes is shown in Table 2, where it can be seen that all frequencies reduce as the aspect ratio is increased, apart from the short period mode. However, it can also be seen that the differences in modal frequency between undeformed and deformed is small, though they increase as the aspect ratio increases.

The Modal Assurance Criterion (MAC)[37] is a method that can be used to quantify similarity of two eigenvectors. In this case, the MAC is carried out between the deformed and undeformed mode shapes as a way to illustrate how linearising the equations about the trimmed geometry can cause different modes to couple. Contour plots of the MAC matrix can be seen in Fig. 7a for the aspect ratio 10 case. There is a strong correlation between the respective modes, indicated by numbers close to 1 on the diagonal. Some off-diagonal contributions can be seen for example, showing how the Dutch Roll mode contains asymmetric first bending and in-plane modes once trimmed geometry is included in the linearisation. Furthermore, the asymmetric bending-plus-engine modes show a strong off-diagonal coupling with the asymmetric in-plane.

The MAC matrix for the aspect ratio 18 (Fig. 7b) shows greater off-diagonal contribution, with stronger coupling of Dutch Roll to in-plane bending modes. In addition, the diagonal entry associated with the asymmetric second bending mode reduces in value, which indicates that this mode is changed significantly by considering the trimmed geometry in the analysis. Interestingly, it can be seen how there is no coupling between in-plane and engine modes that was seen quite strongly in the aspect ratio 10 case.

Finally, the MAC matrix for the aspect ratio 26 case is presented in Fig. 7c. The trend seen from aspect ratio 10 to 18 continues here with greater cross-coupling, and where the contribution of in-plane modes to the Dutch Roll mode increases, and the second bending mode changes with inclusion of the trimmed geometry. From these analyses it can be

Review copy- Do not distribute

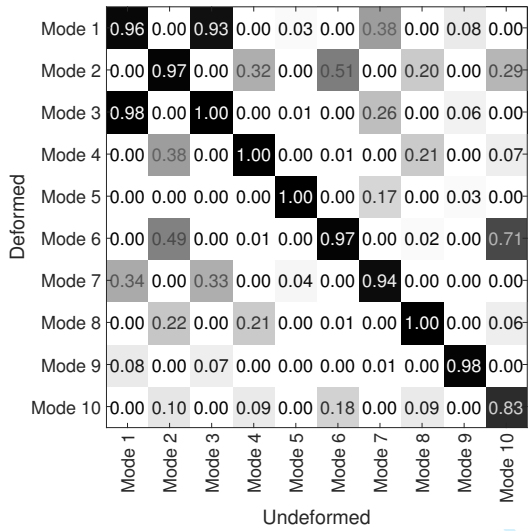

(a) AR 10

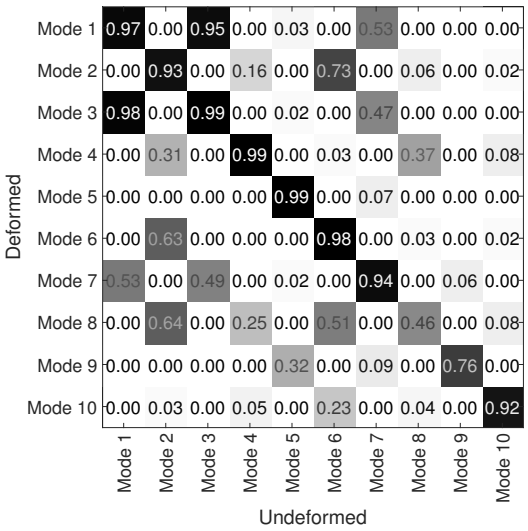

(b) AR 18

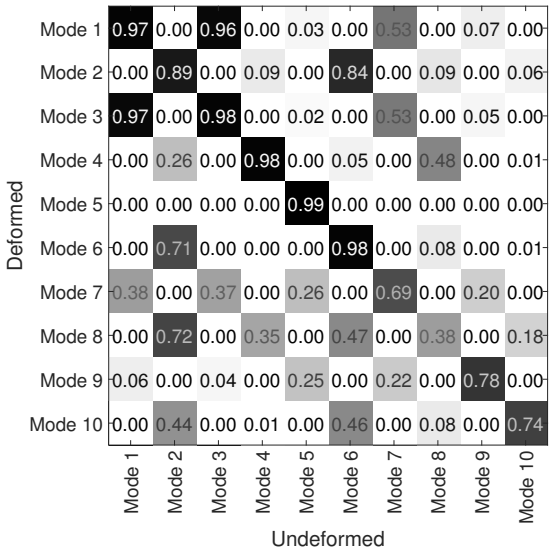

(c) AR 26

Mode 1 = Short Period
Mode 2 = Dutch Roll
Mode 3 = First Bending (Sym)
Mode 4 = First Bending (Asym)
Mode 5 = In-plane (Sym)
Mode 6 = In-plane (Asym)
Mode 7 = Second Bending (Sym)
Mode 8 = Second Bending (Asym)
Mode 9 = Bending + Engine (Sym)
Mode 10 = Bending + Engine (Asym)

Fig. 7 MAC matrix contour plots (Deformed vs. Undeformed)

Review copy- Do not distribute

seen how the impact of trimmed geometry has a more significant effect on the modeshapes of the aircraft as the aspect ratio is increased.

C. Gust Loads Envelopes

First consider the aspect ratio 10 aircraft. Maximum and minimum incremental loads distributions are plotted in Fig. 8 for the aspect ratio 10 aircraft; the loads from purely vertical and lateral gusts are plotted with dashed lines and compared to those calculated from a RTC calculation, plotted with solid lines. Linear simulations, about both the undeformed and trimmed geometries are compared to the full nonlinear simulations. Despite the earlier comments regarding the invalidity of superposition techniques for HARW, the loads minus 1g loads are presented here even for nonlinear loads to focus on the loads purely due to gusts. It can be seen that nonlinearity does not play a significant role with regards to vertical shear and bending loads, where the linear simulations match extremely closely to the nonlinear simulations (whether linearised about the undeformed or trimmed geometries). In the torque loads it can be seen that the root and outboard loads are due to either purely vertical or lateral gusts (dashed lines), but inboard of the engine, there is an increase in loads of around 20% due to a non-vertical (or RTC) gust (solid lines). The torque loads in this region are well predicted by the simulations carried out on the system linearised about the trimmed geometry. The exception to this is close to the root, where a significant difference exists due to an asymmetry between the nonlinear and linearised about the trimmed geometry. When linearised about the undeformed geometry, the root torque loads are over-predicted, and the RTC analyses inboard of the engine are not able to predict the significant increase in loads due to a non-vertical gust. Aside from the quantitative differences, the asymmetry of the maximum and minimum loads can be seen clearly, whereby the maximum and minimum incremental loads from the linear analysis are equal and opposite, but the nonlinear loads are not.

Most noticeably, axial, in-plane shear and in-plane bending loads exhibit very significant differences between the three types of simulation. This effect can be attributed to differences in the way that the aerodynamics is modelled. For example, when linearised about the undeformed geometry, no in-plane or spanwise components of the aerodynamic forces appear in the equations; in turn, the predicted axial and in-plane loads are small (the only contributions to the loads in this direction comes from lateral gust cases inducing yaw motions). If linearised about the appropriate trim condition, the loads in these directions are closer to the nonlinear results, but there are still considerable errors. It can be seen that, even for a low aspect ratio wing, the contribution from in-plane aerodynamic forces affects axial and in-plane loads, and furthermore that this appears to feed through to the torque loads. This emphasises the importance of modelling the aerodynamics correctly, and highlights how drag forces, which are not modelled here and are typically ignored in aeroelastic analyses, could prove to be an important phenomenon in aeroelastic analyses.

For comparison purposes, the gust loads analysis was repeated for the aspect ratio 10 aircraft without engine mass and inertia (see Appendix, Fig. 15). It can be seen that the loads exhibit qualitatively similar behaviour (without the

Review copy- Do not distribute

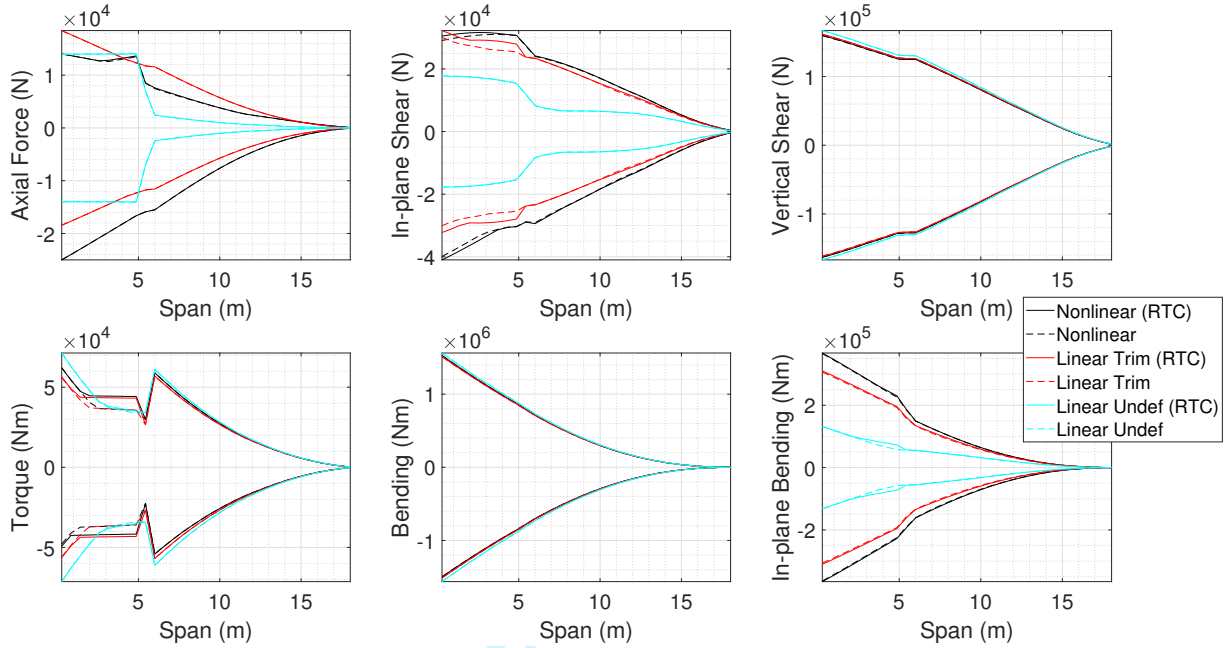

Fig. 8 AR 10 incremental loads distributions with engines.

kink at the engine location) as the case with engines in Fig. 8, aside from the torque loads. Without the engines, the linear torque predictions are much closer to the nonlinear results, but notably worse than in the vertical shear or bending moment loads.

Now consider the gust loads on the aspect ratio 18 case, in Fig. 9. As with the aspect ratio 10 case, the linearised solutions are capable of matching the nonlinear results reasonably well for vertical shear and bending moments. However, the difference between linearised-about-trim and linearised-about-undeformed is more pronounced here, with the linearised-about-undeformed case over-predicting the loads. Torque envelopes display a more significant difference between linear and nonlinear compared to the aspect ratio 10 case, and show that the linear torque envelope at the root underestimates the loads compared to the nonlinear loads (more so in the linearised-about-undeformed than linearised-about-trim). The torque loads here also differ qualitatively from the aspect ratio 10 case, where RTC gusts play a much smaller role for the aspect ratio 18 case. This effect is due to the fact that the engines remain at a fixed distance from the fuselage, and as such, for the aspect ratio 18 case, their dynamics do not couple with bending modes to the degree that they did in the aspect ratio 10 case, i.e., the differences are due to the underlying model characteristics rather than the linearisation.

Finally, consider the gust loads analysis for the aspect ratio 26 case, see Fig. 10. As seen in the lower aspect ratio cases, vertical shear and bending compare well between linear and nonlinear provided the system is linearised about trimmed geometry. When linearised about the undeformed geometry, these loads are over predicted (by around 9% for the root vertical shear loads, for example). Linearised-about-trim results also show a very good match to the nonlinear

Review copy- Do not distribute

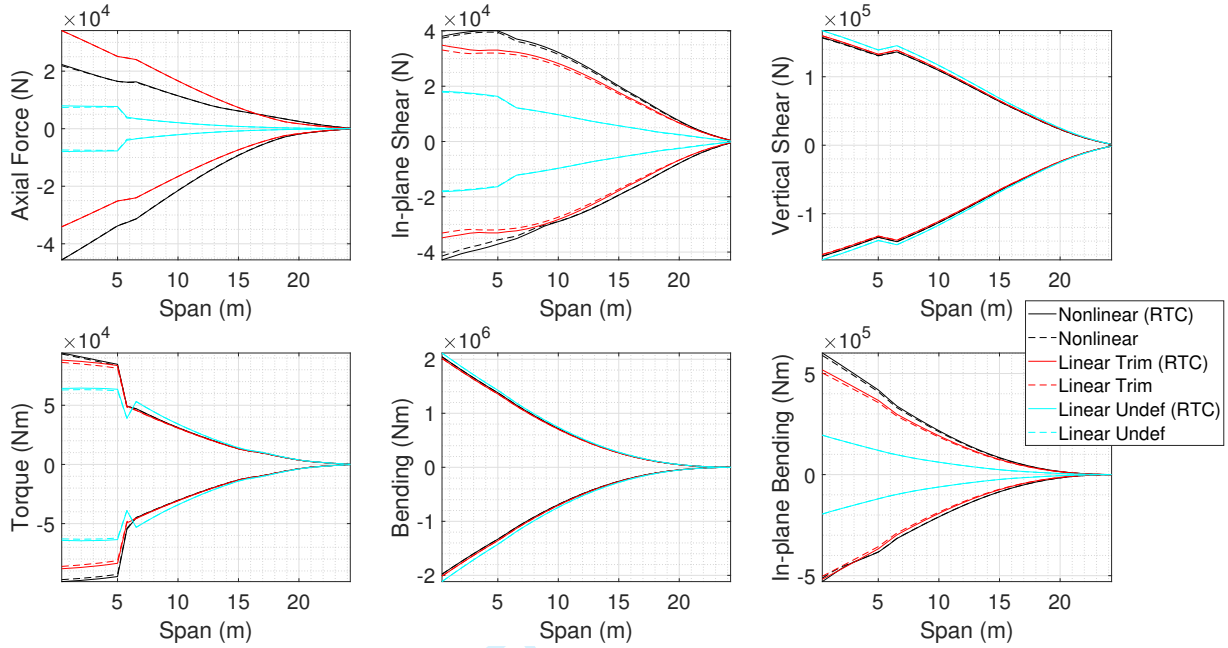

Fig. 9 AR 18 incremental loads distributions.

torque loads, which (in contrast to the vertical shear and bending moments) is significantly under-predicted by the linearised-about-undeformed simulations. This might suggest that the linearised system is predicting the dynamic behaviour of the full nonlinear system well, and much better than for the lower aspect ratio cases. However, closer inspection of the time histories of the torque loads (plotted in Fig. 11 (right) for the worst case gust excitation ($H = 20m$)) reveals that differences in the signals of the linear and nonlinear responses are quite marked, matching up almost coincidentally at a peak around 0.75 seconds, long after the gust has hit the aircraft. Also included in Fig. 11 (left) is the same torque time history subject to a very small gust, indicating that the differences that are seen are indeed due to nonlinearities and not errors in the linearisation.

D. Summary of Linear/Nonlinear Gust Loads Comparisons

The gust loads comparisons are summarised here. They are presented as qualitative observations, but quantitative comparisons can be found in Tables 3 and 4, where the percentage differences of linear results versus nonlinear results at the root have been tabulated for root torque and shear force loads.

Generally, for all aspect ratios considered, vertical shear force and bending moment were predicted very well by the linear system, provided it was linearised about the trimmed geometry. When linearised about the undeformed geometry, vertical shear and bending were over-predicted as compared to the nonlinear results; a trend which is exacerbated by an increased aspect ratio. The tabulated error values for root vertical shear in Tab. 3 show that the error between the linearised and nonlinear simulations increases with aspect ratio when the system is linearised about the undeformed

Review copy- Do not distribute

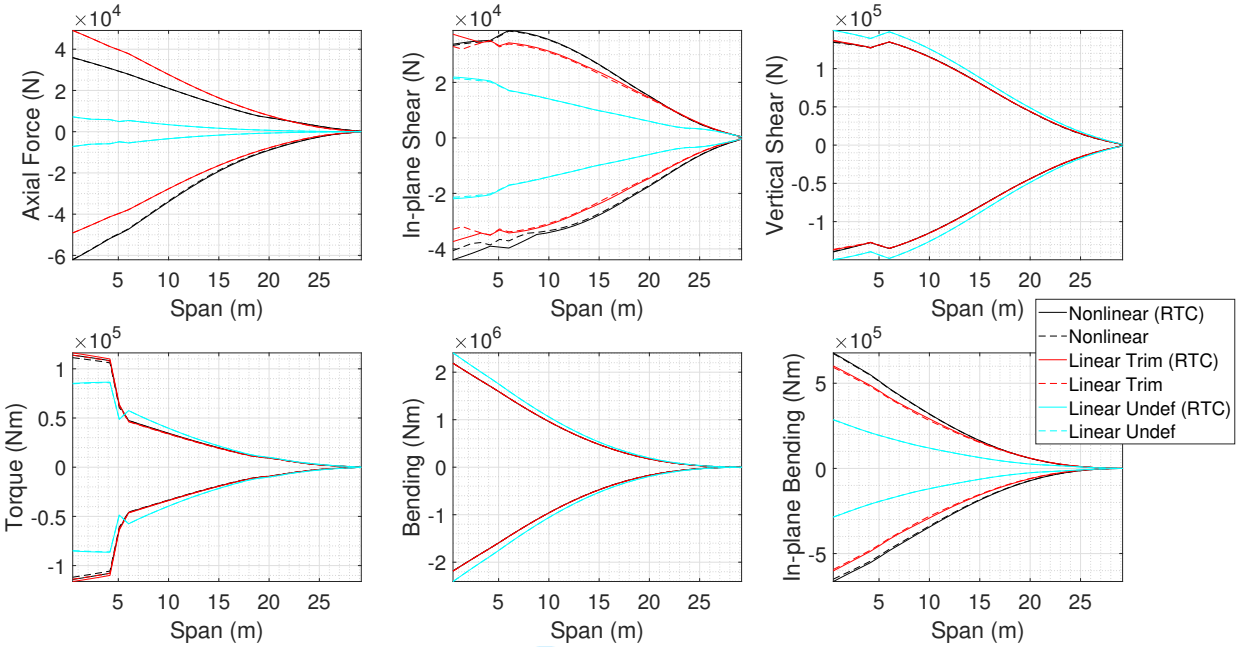

Fig. 10 AR 26 incremental loads distributions.

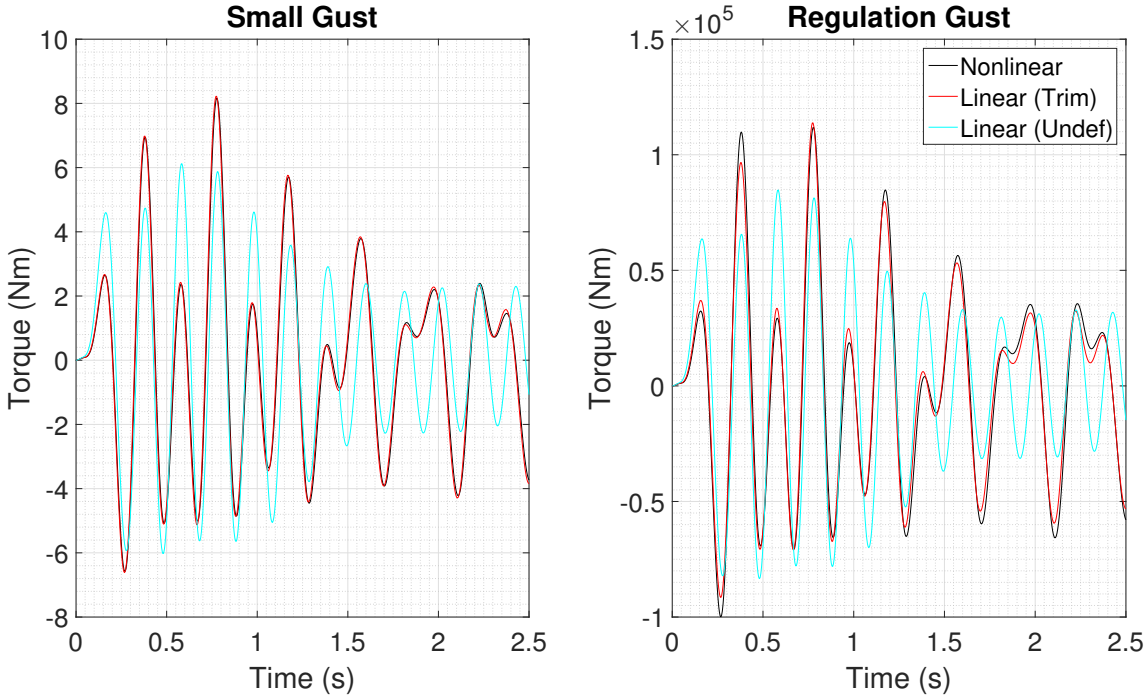

Fig. 11 AR 26 incremental torque time histories.

geometry. However, providing the linearisation is carried out about the trim condition, the error is consistently only ±1 to ±2% for all aspect ratios.

General observations can also be made about axial, in-plane bending and in-plane shear loads for all aspect ratios, inasmuch as they are more or less consistently under-predicted by the linear system. Providing the linearisation is carried out about the trimmed geometry the prediction is better, but nonetheless does not capture the full dynamic behaviour.

Finally, torque loads proved to be the least easy to generalise, and are very dependent on the aspect ratio. Interestingly, significant nonlinear effects were observed even on the aspect ratio 10 case with engine; a low aspect ratio case such as this would not typically be thought to exhibit strong nonlinearities. From the tabulated error values for root torque in Tab. 4, the differences that are seen between the linearised and nonlinear simulations do not lead to a concise conclusion about the relative behaviour; on some aspect ratios the torque is over-predicted while under-predicted for another. The linear system appears to provide increasingly better predictions of the nonlinear loads envelope as the aspect ratio increases, contrary to what might be expected. However, it appears that this is not a phenomenon that could be guaranteed for a different model. The asymmetry of the maximum versus minimum torque loads for the nonlinear system can also be seen in Tab. 4, where the differences between maximum and minimum loads show significantly different magnitudes as compared to the vertical shear loads as in Tab. 3.

	Aspect Ratio	1g Vertical Shear (N)	Incremental Root Vertical Shear Gust Load (N)	Root Load Percentage difference vs. Nonlinear Root Loads (%)	
				Linearised about undeformed	Linearised about trim
Max Load	10	2.13×10^5	1.59×10^5	4.40	1.12
	18	2.24×10^5	1.57×10^5	6.43	1.64
	26	2.34×10^5	1.35×10^5	11.00	1.59
Min Load	10	2.13×10^5	-1.63×10^5	2.28	-0.94
	18	2.24×10^5	-1.62×10^5	3.21	-1.44
	26	2.34×10^5	-1.40×10^5	7.41	-1.70

Table 3 Root Vertical Shear Percentage Error Compared to Nonlinear

E. Round-the-Clock Gust Loads

While the peak loads for the RTC gusts were presented in the last section, here we examine the variation of these loads with gust angle. Polar plots of the maximum torque loads for a particular gust direction are plotted in Fig. 12, comparing the linear and nonlinear calculations for torque at the root of the wing, and at approximately 3.5m outboard, just inboard of the engines. The solid lines in Fig. 12 were generated from the left wing, and it can be seen how there is no left-right symmetry. This is because the envelope is for the maximum load. The envelope for the right wing is also included for the nonlinear results, as a dashed line, to illustrate that this is a left-right mirror of the left wing envelopes.

Review copy- Do not distribute

	Aspect Ratio	1g Torque (Nm)	Incremental Root Torque Gust Load (Nm)	Root Load Percentage difference vs. Nonlinear Root Loads (%)	
				Linearised about undeformed	Linearised about trim
Max Load	10	-8.23×10^4	6.22×10^4	14.82	-9.27
	18	-4.94×10^4	9.42×10^4	-31.79	-6.38
	26	-2.08×10^4	1.14×10^5	-25.15	2.04
Min Load	10	-8.23×10^4	-4.92×10^4	44.93	14.52
	18	-4.94×10^4	-9.90×10^4	-35.14	-10.98
	26	-2.08×10^4	-1.14×10^5	-25.36	1.77

Table 4 Root Torque Percentage Error Compared to Nonlinear

Figure 12a shows that the maximum torque loads at the root compare for the aspect ratio 10 case results for nonlinear versus linear simulations. It can be seen that the maximum root gust torque predicted by the nonlinear code is due to a slightly off-vertical gust (highlighted with a cross at about -7.5° from vertical). This is also captured reasonably closely by the linearised-about-trim case, but when linearised about the undeformed geometry, a gust closer to only 2° from vertical induces the maximum root torque. However, the torque for other gust directions shows a significant difference between the methods. A similar plot in Fig. 12d illustrates the same torque envelope at approximately 3.5m outboard, where the worst case gust direction is shown to be around -130°. The linear analysis carried out about the trimmed geometry predicts the same direction for the worst case gust torque, but the linear analysis about the undeformed still predicts a much more vertical gust as the worst case, at around -13° from vertical.

Polar plots of the maximum torque loads for a particular gust direction for aspect ratios 18 and 26 are also shown in Fig. 12. For both aspect ratio 18 and 26, the maximum torque for the nonlinear system is predicted to be due to a slightly off-vertical gust (roughly in the ±10° range). The linearised-about-trim results also predict this worst case direction, but under predicts the magnitude of the loads in this direction for the aspect ratio 18 case while matching it well for the aspect ratio 26 case. The worst case gust direction for torque predicted by the linear-about-undeformed simulation is in the complete opposite direction for aspect ratio 18, at both at the root and in-board of the engine, at around 170°. This is most likely due to differences in the aerodynamic damping due to the deformations for the linearised-about-undeformed case which will affect the pitching motion and in turn could cause the worst case loads to occur post-gust. Also, the torque envelope in all directions for the linearised-about-undeformed simulation is greatly reduced compared to the linear.

As the aspect ratio increases, the impact of lateral gusts at approximately 3.5m outboard is seen to reduce dramatically, which can be attributed to a decoupling of the torsional and in-plane bending modes as the aspect ratio increases, with the engines remaining at a fixed distance from the fuselage.

In addition to the torque polar plots shown in Fig. 12, polar plots showing the maximum bending moment for a

For Peer Review

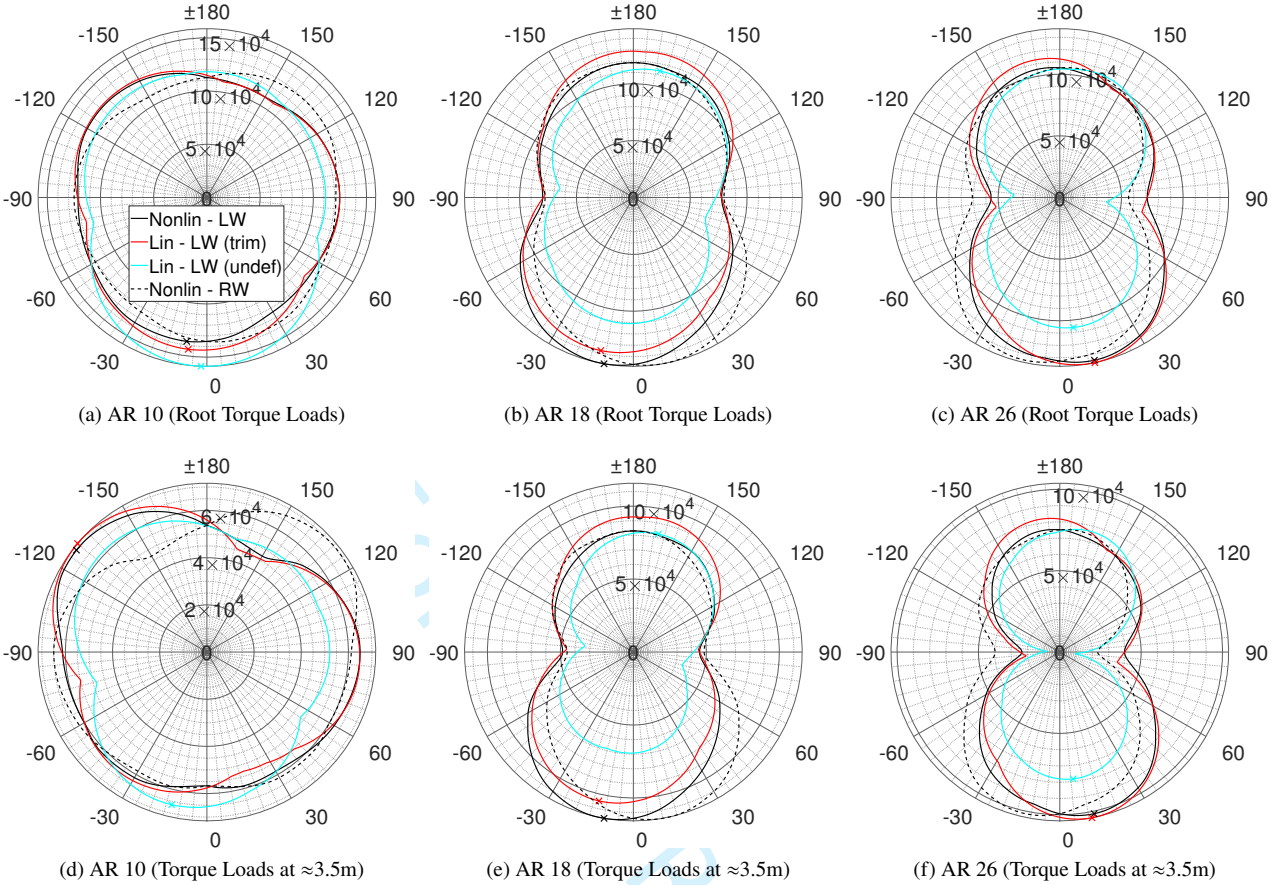

Fig. 12 Polar plot of maximum absolute total torque loads for a particular gust direction (crosses highlight maxima). LW = left wing; RW = right wing.

particular gust direction are plotted in Fig. 13. In contrast to the torque plots, it can be seen that the vertical gust is close to the worst case for all aspect ratios. For the aspect ratio 10 case, Fig. 13a, the vertical gust is significantly higher than any other gust direction, but as the aspect ratio increases, the loads due to a negative gust (at θ=180°) approach those of the vertical gust, with the negative gust generating slightly loads for the aspect ratio 26 case. The linear results match the nonlinear well, in terms of magnitude and worst case gust direction.

As well as the torque plots, the worst case root bending differs between left and right wing (compare solid and dashed black lines in Fig. 12) however, the effect is much less marked than for the torque.

F. Correlated Loads

So far, only 1D envelopes have been considered, whereby the maximum and minimum of a given load is calculated for all gust disturbances, for all timesteps simulated, and plotted as distributions along the span. It is also required to capture the behaviour of correlated loads (e.g. bending moment and torque measured at concurrent time instances) to provide design loads for 3D FE analysis. This requirement is achieved by plotting the response of loads, to all the gust

Review copy- Do not distribute

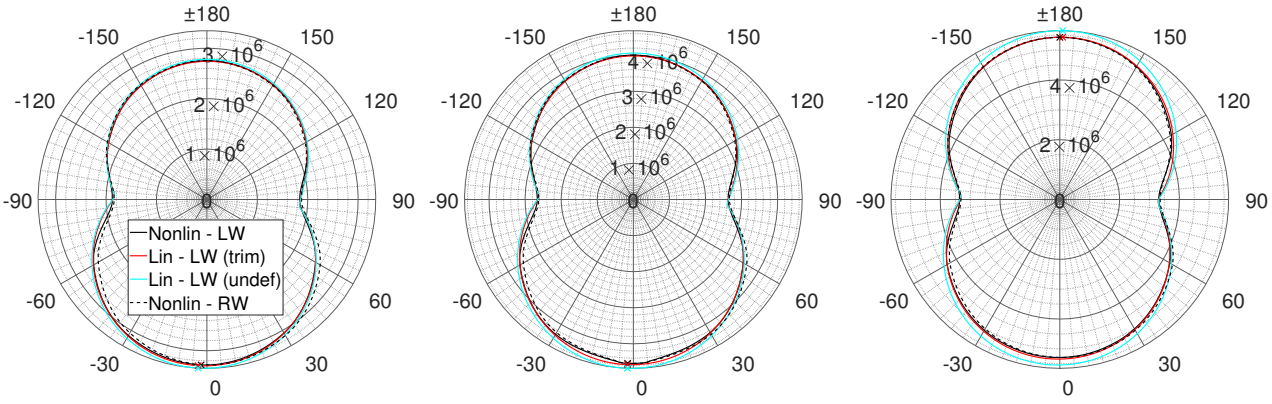

(a) AR 10 (Root Bending Loads) (b) AR 18 (Root Bending Loads) (c) AR 26 (Root Bending Loads)

Fig. 13 Polar plot of maximum absolute total bending moment for a particular gust direction (crosses highlight maxima). LW = left wing; RW = right wing.

excitations, against one another for each time point and then computing the "convex hull", which is the envelope of all the correlated time traces[5].

Figure 14 shows torque versus bending moment correlated loads envelopes for the three different aspect ratio wings (negative torque is wing pitch-up, negative bending is wing-up bending, in this case). For the aspect ratio 10 case (Fig. 14a) the linearised-about-trim results show a comparable envelope to the nonlinear results, but for a small shift in torque, whereas the linearised-about-undeformed envelope is significantly skewed and over predicts the envelope. As the aspect ratio is increased to 18 and 26 (Figs. 14b and 14c, respectively), the linearised-about-undeformed begins to under predict the loads envelopes, while the linear-about-trim still provides a reasonable match to the nonlinear results. This is consistent with the results seen for the envelope distributions, and indicates that the linear model is capable of predicting the correlated loads quite well, providing they are linearised about the trim shape.

V. Conclusions

Round-the-clock gust load analysis has been performed using three variants of a conceptual commercial aircraft featuring aspect ratios of 10, 18 and 26, with their internal structures determined from an industrial-style sizing process based on static loads simulations to ensure the structure is both structurally sound, and with a minimized mass. Analyses were carried out using an aeroelastic framework, using a geometrically-exact nonlinear beam formulation and linear unsteady aerodynamics, applied to a gust loads process based on industrial practices defined for use on a linear system, but adapted for use on a nonlinear system. Simulations were carried out for all three aspect ratios in order to understand how results obtained from a full, geometrically-exact nonlinear analysis compare to the results from a linearised system.

Stability analysis carried out on the linear systems showed how bending modes reduced in frequency, while increasing in damping as aspect ratio increases (at the flight case considered). The real and imaginary parts of these modes agreed

For Peer Review

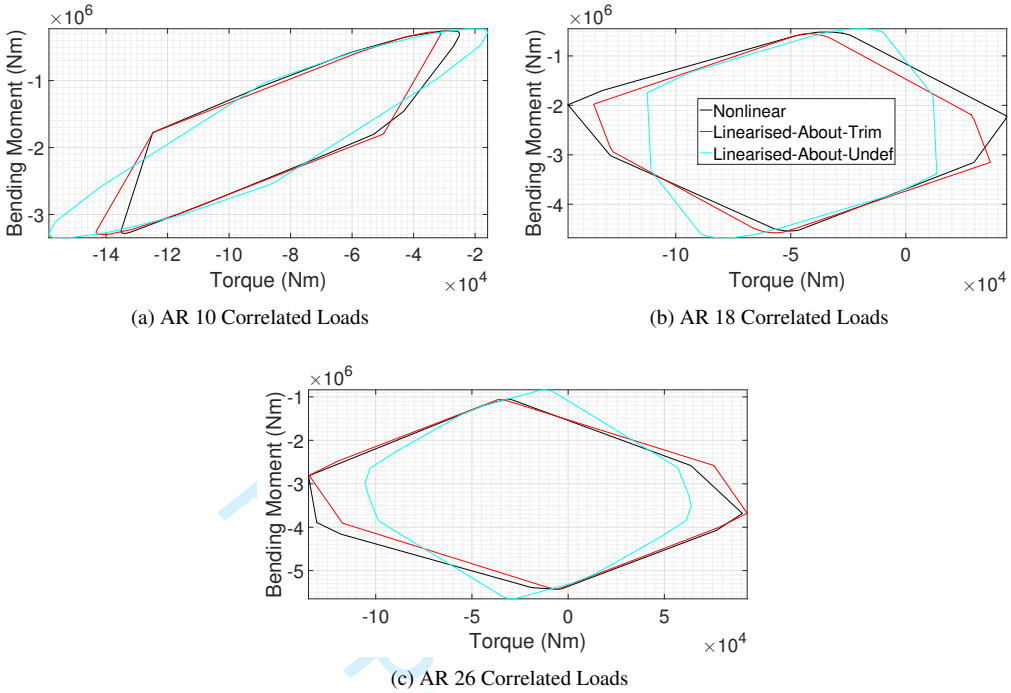

(a) AR 10 Correlated Loads

(b) AR 18 Correlated Loads

(c) AR 26 Correlated Loads

Fig. 14 Correlated Loads showing the convex hull of all time histories of torque vs. bending moment.

well between linearised-about-undeformed and linearised-about-trim for the aspect ratio 10 cases, but began to differ as the aspect ratio was increased. However, some modes, primarily in-plane and torsional (i.e. the engine+bending mode), exhibited different real and imaginary parts even for low aspect ratio cases. This finding implied that linearising the equations about the undeformed geometry is only satisfactory if considering bending behaviour of low aspect ratio aircraft and the torsional modes do not interact significantly with them. Otherwise, the state about which the equations are linearised is important to the results, even for low aspect ratio wings.

Overall, vertical shear force and bending moment show very little nonlinear behaviour, whereas in-plane loads are significantly under-predicted under linear assumptions for this particular class of aircraft. The effect of nonlinearities on torque is shown to be very problem-dependent, and it is not easy to say *a priori* whether a linear assumption would over or under-predict torque. It was particularly interesting to see how geometric nonlinearities became important in the prediction of torque loads for the aspect ratio 10 case, indicating that even lower aspect ratio aircraft cannot be simply assumed to be structurally linear. Conversely, as the aspect ratio was increased, torque loads between the linear and nonlinear approaches began to agree much more closely, but from the analysis it was suggested that this is not likely to be a universal trend. Results in this study show how important in-plane components of force are on the loads behaviour, despite the fact only linear, incompressible, inviscid aerodynamics was used in this work. This finding suggests that drag, be it viscous, lift-induced or transonic shock based drag components, may prove important in the loads analysis, particularly considering drag is usually ignored in traditional aeroelastic loads studies.

Review copy- Do not distribute

Appendix

A. Intrinsic Beam Theory

To begin the beam description[11], one considers a beam described simply by a 1D coordinate, s, along the deformed beam's length. It is first necessary to define the variables that are used in the formulation. First, local strain, $\boldsymbol{\gamma}_B(s,t) \in \mathbb{R}^{3\times1}$, and curvature, $\boldsymbol{\kappa}_B(s,t) \in \mathbb{R}^{3\times1}$, are defined as

$$\boldsymbol{\gamma}_B(s,t) = [C^{Ba}(s,t)]\boldsymbol{R}_a(s,t)' - \boldsymbol{e}_1 \tag{2}$$

and

$$\tilde{\boldsymbol{\kappa}}_B(s,t) = [C^{Ba}(s,t)][C^{aB}(s,t)]', \tag{3}$$

respectively. In these equations, $\boldsymbol{R}_a(s,t) \in \mathbb{R}^{3\times1}$ is the position vector to any point on the aircraft structure as seen in the body-fixed reference frame, a, and $[C^{Ba}(s,t)] \in \mathrm{SO}(3)$ is a rotation matrix mapping a vector in frame a to frame B. The vector $\boldsymbol{e}_1$ is a constant, defined as $\boldsymbol{e}_1 := [\,1\;0\;0\,]^T$ and the $\bullet'$ operator represents the spatial derivative of a certain variable with respect to s, while the $\tilde{\bullet}$ represents the cross-product matrix operator of a given vector. Pre-strains, $\boldsymbol{\gamma}_{B_0}(s,t)$ and pre-curvatures, $\boldsymbol{\kappa}_{B_0}(s,t)$ could be added to Eqns (2) and (3), respectively, but are neglected here for clarity since they are not used.

Further to these strain and curvature definitions, the local translational velocity, $\boldsymbol{V}_B(s,t) \in \mathbb{R}^{3\times1}$, and angular velocity, $\boldsymbol{\Omega}_B(s,t) \in \mathbb{R}^{3\times1}$, are defined as

$$\boldsymbol{V}_B(s,t) = [C^{Ba}(s,t)]\left(\dot{\boldsymbol{R}}_a(s,t) + \tilde{\boldsymbol{\omega}}_a(t)\boldsymbol{R}_a(s,t) + \boldsymbol{v}_a(t)\right) \tag{4}$$

and

$$\tilde{\boldsymbol{\Omega}}_B(s,t) = [C^{Ba}(s,t)][\dot{C}^{aB}(s,t)] + [C^{Ba}(s,t)]\tilde{\boldsymbol{\omega}}_a(t)[C^{aB}(s,t)], \tag{5}$$

respectively, where $\boldsymbol{v}_a \in \mathbb{R}^{3\times1}$ is the translational velocity of the body-fixed reference frame, and $\boldsymbol{\omega}_a \in \mathbb{R}^{3\times1}$ is the rotational velocity. The $\dot{\bullet}$ operator represents the temporal derivative of a certain variable. From this point on, the subscript B will be dropped from the velocities, strains and curvatures for clarity, as well as explicit mention that they are functions of beam location, s, or time, t.

The matrices $[M(s)] \in \mathbb{R}^{6\times6}$ and $[C(s)] \in \mathbb{R}^{6\times6}$ are introduced as the sectional mass (symmetric) and compliance matrices, respectively, and are given as

$$\begin{Bmatrix}\boldsymbol{P}\\ \boldsymbol{H}\end{Bmatrix} = [M]\begin{Bmatrix}\boldsymbol{V}\\ \boldsymbol{\Omega}\end{Bmatrix} = \begin{bmatrix} mI & -m\tilde{\boldsymbol{\xi}} \\ m\tilde{\boldsymbol{\xi}} & J \end{bmatrix}\begin{Bmatrix}\boldsymbol{V}\\ \boldsymbol{\Omega}\end{Bmatrix} \quad \text{and} \quad \begin{Bmatrix}\boldsymbol{\gamma}\\ \boldsymbol{\kappa}\end{Bmatrix} = [C]\begin{Bmatrix}\boldsymbol{F}\\ \boldsymbol{M}\end{Bmatrix} = \begin{bmatrix} c_{\gamma f} & c_{\gamma m} \\ c_{\kappa f} & c_{\kappa m} \end{bmatrix}\begin{Bmatrix}\boldsymbol{F}\\ \boldsymbol{M}\end{Bmatrix} \tag{6}$$

For Peer Review

which map velocities to translational and rotational momenta, $\boldsymbol{P}$ and $\boldsymbol{H}$, respectively, and forces, $\boldsymbol{F}$, and moments, $\boldsymbol{M}$, to strains and curvatures. In the sectional mass matrix, $m(s) \in \mathbb{R}$ and $J(s) \in \mathbb{R}^{3\times3}$ are the sectional mass and rotational inertia of the beam per unit length, respectively, and $\boldsymbol{\xi} \in \mathbb{R}^3$ is the mass offset, defined in the beam-fixed reference frame sign convention. In the sectional compliance matrix, $c_{ij} \in \mathbb{R}^{3\times3}$ simply refers to submatrices of the full matrix, with more detail available on obtaining this in Ref. [38]. It can be seen that the relationship between the beam forces and moments, and the strains and curvatures is linear, indicating that there are no material nonlinearities such as skin-buckling or plasticity accounted for in this method.

The equations of motion of the beam, in strong form, are rewritten from Hodges[11] as,

$$[M]\begin{Bmatrix}\dot{\boldsymbol{V}}\\ \dot{\boldsymbol{\Omega}}\end{Bmatrix}+\begin{bmatrix}\tilde{\boldsymbol{\Omega}} & 0\\ \tilde{\boldsymbol{V}} & \tilde{\boldsymbol{\Omega}}\end{bmatrix}[M]\begin{Bmatrix}\boldsymbol{V}\\ \boldsymbol{\Omega}\end{Bmatrix}=\begin{Bmatrix}\boldsymbol{F}'\\ \boldsymbol{M}'\end{Bmatrix}-\begin{bmatrix}0 & \tilde{\boldsymbol{F}}\\ \tilde{\boldsymbol{F}} & \tilde{\boldsymbol{M}}\end{bmatrix}[C]\begin{Bmatrix}\boldsymbol{F}+\boldsymbol{e}_f\\ \boldsymbol{M}\end{Bmatrix}+\begin{Bmatrix}\boldsymbol{f}\\ \boldsymbol{m}\end{Bmatrix}, \tag{7}$$

where $\boldsymbol{e}_f = c_{\gamma f}\boldsymbol{e}_1$, and $\boldsymbol{f}$ and $\boldsymbol{m}$ are local, externally applied forces and moments, respectively.

In Eq. (7), the degrees of freedom of the equations of motion are local velocities and strains and curvatures. In contrast to similar methods which rewrite the equations of motion purely in terms of strains and curvatures, or alternatively in terms of displacements and orientations, the intrinsic beam approach introduces an additional equation which relates the velocities to the strain and curvatures, which closes the formulation. This equation is derived from Eqs. (2) and (3), as

$$[C]\begin{Bmatrix}\dot{\boldsymbol{F}}\\ \dot{\boldsymbol{M}}\end{Bmatrix}=\begin{Bmatrix}\boldsymbol{V}'\\ \boldsymbol{\Omega}'\end{Bmatrix}-\begin{bmatrix}\tilde{\boldsymbol{\Omega}} & \tilde{\boldsymbol{V}}\\ 0 & \tilde{\boldsymbol{\Omega}}\end{bmatrix}[C]\begin{Bmatrix}\boldsymbol{F}+\boldsymbol{e}_f\\ \boldsymbol{M}\end{Bmatrix}. \tag{8}$$

Equations (7) and (8) are transformed into their weak form, and rewritten concisely as follows,

$$\int_0^t\int_0^l \delta\boldsymbol{y}(s,t)^T([A_0]\dot{\boldsymbol{x}}(s,t)-[A_1]\boldsymbol{x}'(s,t)-[A_2(s)](\boldsymbol{x}(s,t)\otimes\boldsymbol{x}(s,t))-[A_3]\begin{Bmatrix}\boldsymbol{f}(s,t)\\ \boldsymbol{m}(s,t)\end{Bmatrix})\mathrm{d}s\mathrm{d}t=0 \tag{9}$$

where $\boldsymbol{x} = [\boldsymbol{F};\boldsymbol{M};\boldsymbol{V};\boldsymbol{\Omega}] \in \mathbb{R}^{12}$ is a vector of the beam loads and velocities, and $\delta\boldsymbol{y} = [\delta\boldsymbol{R};\delta\boldsymbol{\Phi};\delta\boldsymbol{I};\delta\boldsymbol{J}] \in \mathbb{R}^{12}$ is the vector of infinitesimal displacements, rotations and force and impulse variations. The matrices $[A_1] \in \mathbb{R}^{12\times12}$ and $[A_2] \in \mathbb{R}^{12\times12^2}$ are system matrices derived from rearranging Eqns. (7) and (8), and the matrix $[A_3] \in \mathbb{R}^{12\times6}$ pads the vector of applied forces and moments out with zeros to apply it only to Eq. (7). The $\otimes$ operator is the Kronecker product, where it should be noted that because numerous columns of $[A_2]$ are all zero, using the Kronecker product in this way may not be the most computationally efficient approach, but nonetheless provides a very concise way to summarise the equations, and highlights clearly how the highest degrees of nonlinearity in the intrinsic beam approach are quadratic. A

Review copy- Do not distribute

finite element discretisation of Eq. (9) is achieved by introducing shape function approximations to the state vector $\boldsymbol{x}$ and infinitesimal variations $\delta\boldsymbol{y}$, and integrating out the matrices. The following shape functions are introduced,

$$\boldsymbol{x}(s,t) = [N(s)]\,\bar{\boldsymbol{x}}(t) \quad \text{and} \quad \delta\boldsymbol{y}(s,t) = [W(s)]\,\delta\bar{\boldsymbol{y}}(t), \tag{10}$$

defined such that the appropriate boundary conditions are satisfied (i.e. $\delta\boldsymbol{R}(0) = \delta\boldsymbol{\Phi}(0) = \boldsymbol{F}(l) = \boldsymbol{M}(l) = 0$ and $\delta\boldsymbol{I}(l) = \delta\boldsymbol{J}(l) = \boldsymbol{V}(0) = \boldsymbol{\Omega}(0) = 0$ for a cantilever beam for example). Additional shape functions, $[N_{pt}(s)]$ and $[N_{dst}(s)]$ are introduced which describe the force and moment distributions; here only point loads (engine thrust) and distributed loads (aerodynamics and gravity) are required. The shape functions for the applied loads are given as

$$\begin{Bmatrix} \boldsymbol{f}(s,t) \\ \boldsymbol{m}(s,t) \end{Bmatrix} = \big[N_{pt}(s)\big] \begin{Bmatrix} \boldsymbol{f}_{pt}(t) \\ \boldsymbol{m}_{pt}(t) \end{Bmatrix} + [N_{dst}(s)] \begin{Bmatrix} \boldsymbol{f}_{dst}(t) \\ \boldsymbol{m}_{dst}(t) \end{Bmatrix}, \tag{11}$$

where $\boldsymbol{f}_{pt}$ and $\boldsymbol{m}_{pt}$ are vectors of various point forces and moments, respectively, and $\boldsymbol{f}_{dst}$ and $\boldsymbol{m}_{dst}$ are the control points of distributed force and moments, respectively. The shape function, $[N_{pt}]$, is essentially a matrix of shifted Dirac delta functions to apply point loads at the appropriate location on the beam.

The final FE formulation for the beam can be written as

$$[B_0]\dot{\bar{\boldsymbol{x}}}(t) = [B_1]\bar{\boldsymbol{x}}(t) + [B_2](\bar{\boldsymbol{x}}(t) \otimes \bar{\boldsymbol{x}}(t)) + [B_3] \begin{Bmatrix} \boldsymbol{f}_{pt}(t) \\ \boldsymbol{m}_{pt}(t) \end{Bmatrix} + [B_4] \begin{Bmatrix} \boldsymbol{f}_{dst}(t) \\ \boldsymbol{m}_{dst}(t) \end{Bmatrix} + [\bar{\boldsymbol{x}}]_0^l, \tag{12}$$

where $[B_0] = \int_0^l [W(s)]^T [A_0][N(s)]\mathrm{d}s$, $[B_3] = \int_0^l [W(s)]^T [N_{pt}(s)]\mathrm{d}s$, $[B_4] = \int_0^l [W(s)]^T [N_{dst}(s)]\mathrm{d}s$, and

$$[B_1] = -\int_0^l [W(s)]'^T [A_1][N(s)]\mathrm{d}s \quad \text{and} \quad [B_2] = \int_0^l [W(s)]^T [A_2(s)]([N(s)] \otimes [N(s)])\mathrm{d}s, \tag{13}$$

The first equation in Eq. (13), along with additional boundary conditions, $[\bar{\boldsymbol{x}}]_0^l$, in Eq. (12) are results of integration by parts of the spatial derivative term in Eq. (9). The second equation uses a property of Kronecker products (i.e. $AB \otimes CD = (A \otimes C)(B \otimes D)$) which can easily apply the shape functions without changing the form of the expressions in Eq. (9).

One final equation of motion is required for the free-flying aircraft,

$$\int_0^l \begin{bmatrix} I & 0 \\ \tilde{\boldsymbol{R}}_a & I \end{bmatrix} \begin{bmatrix} C^{aB} & 0 \\ 0 & C^{aB} \end{bmatrix} \left([M] \begin{Bmatrix} \dot{\boldsymbol{V}} \\ \dot{\boldsymbol{\Omega}} \end{Bmatrix} + \begin{bmatrix} \tilde{\boldsymbol{\Omega}} & 0 \\ \tilde{\boldsymbol{V}} & \tilde{\boldsymbol{\Omega}} \end{bmatrix} [M] \begin{Bmatrix} \boldsymbol{V} \\ \boldsymbol{\Omega} \end{Bmatrix} - \begin{Bmatrix} \boldsymbol{f} \\ \boldsymbol{m} \end{Bmatrix} \right) \mathrm{d}s = \boldsymbol{0}, \tag{14}$$

which satisfies the conservation of momentum equations for the beam, or set of beams, in the G reference frame. It can

Review copy- Do not distribute
For Peer Review

be seen that the translational and rotational velocities of the body-fixed reference frame, $\boldsymbol{v}_a$ and $\boldsymbol{\omega}_a$, respectively, are not solved for directly in Eq. (14), and these variables do not appear explicitly, but remain embedded within the variables $\boldsymbol{V}$ and $\boldsymbol{\Omega}$ (see Eqs. (4) and (5)). Instead, Eq. (14) is treated more like a Lagrange multiplier constraint on the beam equations, where the velocity of the rigid body is coupled with the beam equation as a velocity boundary condition on Eq. (12) at the root, and they are solved simultaneously to satisfy both equations.

The intrinsic beam formulation results in double the number of variables compared to alternative nonlinear beam approaches, but in doing so retains a much more algebraically simple set of equations to solve, as can be seen from the simplicity of Eq. (9). Palacios *et al.*[21] compare the intrinsic beam formulation to two common approaches to nonlinear beam modelling, namely displacement-based[6] and strain-based methodologies[8], and highlight benefits and drawbacks of each method. The simplicity of the intrinsic beam equations can be seen to be advantageous computationally. A finite-element (FE) approach to the solution of the intrinsic beam equations is applied. Here, a similar scheme to those used in Hodges *et al.*[38] is employed, whereby the shape functions for the velocities and state variations are piecewise-linear, and the shape functions for the beam loads are piecewise constant for a given structural element. Using this approach, a discretisation of the beam, or set of beams, into n elements results in a state vector, $\bar{\boldsymbol{x}} \in \mathbb{R}^{12n\times 1}$, and the shape functions, $[N(s)], [W(s)] \in \mathbb{R}^{12\times 12n}$.

However, rather than using a mixed-formulation, the intrinsic beam equations are solved for velocities and beam loads directly. The position and orientation of the beam are still required for the simulations as can be seen specifically in Eq. 14, and in order to rotate globally defined gust velocity and gravity vectors into the local frames of references; these additional values can be obtained by one of two methods. Due to the choice of piecewise constant shape functions for the beam loads, the spatial integration of the strains and curvatures can be achieved using an iterative approach based on rearranging and integrating Eqns. (2) and (3) using a matrix exponential in the following way[8],

$$\begin{bmatrix} \boldsymbol{R}_a(s) & C^{aB}(s) \end{bmatrix} = \begin{bmatrix} \boldsymbol{R}_a(s_n) & C^{aB}(s_n) \end{bmatrix} \mathrm{e}^{[K]_n(s-s_n)} \quad \text{for} \quad \forall s \in \begin{bmatrix} s_n, s_{n+1} \end{bmatrix} \tag{15}$$

where

$$[K]_n = \begin{bmatrix} 0 & 0 \\ \boldsymbol{\gamma}_n + \boldsymbol{e}_1 & \tilde{\boldsymbol{\kappa}}_n \end{bmatrix}, \tag{16}$$

and the initial values of position, $\boldsymbol{R}_a(0)$, and orientation, $\left[C^{aB}(0)\right]$, are defined by the problem definition (static angle of attack or bank angle, etc.). This method is used in the core of the formulation of Cesnik and Brown[8], Shearer and Cesnik[9] and Su and Cesnik[10], and can be re-written using the Cayley-Hamilton theorem to increase computational efficiency[9]. However, in the dynamic simulations, temporal integration of the velocities is favoured to avoid repeated calls to computationally expensive exponential or trigonometric functions. In this work, the orientations of the beam are parameterised using quaternions, which leads to the following ODEs which can be solved in addition to Eqs 12 and 14,

Review copy- Do not distribute
For Peer Review

such that,

$$\dot{\boldsymbol{R}}_G = [C^{GB}]\boldsymbol{V}_B \quad \text{and} \quad \dot{\boldsymbol{\zeta}} = -\frac{1}{2}\begin{bmatrix} 0 & \boldsymbol{\Omega}_B^T \\ -\boldsymbol{\Omega}_B & \tilde{\boldsymbol{\Omega}}_B \end{bmatrix}\boldsymbol{\zeta}. \tag{17}$$

where $\boldsymbol{\zeta} = [\zeta_0; \zeta_1; \zeta_2; \zeta_3] = [\zeta_0; \bar{\boldsymbol{\zeta}}^T] \in \mathbb{R}^{4\times 1}$ is a vector of the Euler parameters that represent the quaternion, $\zeta \in \mathbb{H}$. The rotation matrix for a given node of the problem, $[C^{GB}]$, can be obtained efficiently from the quaternion parameters, where $[C^{GB}] = [H_+(\boldsymbol{\zeta})][H_-(\boldsymbol{\zeta})]^T$ in which $[H_\pm] = \begin{bmatrix} -\bar{\boldsymbol{\zeta}} & \zeta_0 I \pm \tilde{\bar{\boldsymbol{\zeta}}} \end{bmatrix} \in \mathbb{R}^{3\times 4}$[15] (this approach does not require iterative calls to exponential functions as in Eq. 15). The rotation matrix of the body-fixed reference point,$[C^{Ga}]$, can be found simply by evaluating Eqns. 17 at the location of that particular reference point. Additional rotation matrices required in the formulation can be determined using properties of SO(3) matrices (e.g. $[C^{aB}] = [C^{aG}][C^{GB}] = [C^{Ga}]^T[C^{GB}]$).

B. Extra Results

Results from the aspect ratio wing 10 case without engines is included here (Fig. 15) for direct comparison with the results with engines (Fig. 8) to highlight the effect of the engines.

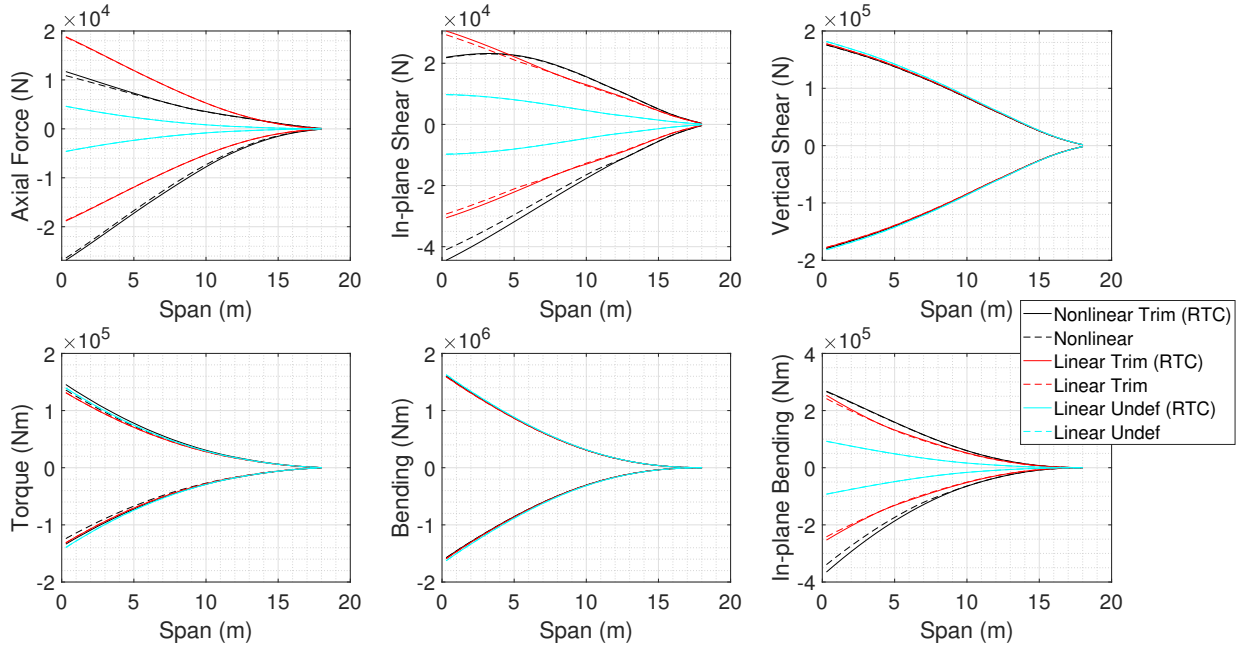

Fig. 15 AR 10 incremental loads distributions without engines.

Acknowledgments

The research leading to these results has been supported by the Agile Wing Integration Innovate UK Aerospace Technology Institute (ATI) project (TSB-113041) and the AEROGUST project (funded by the European Commission

Review copy- Do not distribute

under grant agreement number 636053). In addition, J. E. Cooper is supported by the Royal Academy of Engineering, and S. A. Neild by EPSRC fellowship EP/K005375/1.

References

[1] Noll, T. E., Ishmael, S. D., Henwood, B., Perez-Davis, M. E., Tiffany, G. C., Gaier, M., Brown, J. M., and Wierzbanowski, T., "Technical findings, lessons learned, and recommendations resulting from the Helios prototype vehicle mishap," *NATO/RTO AVT-145 Workshop on Design Concepts, Processes and Criteria for UAV Structural Integrity*, Florence, Italy, 2007.

[2] "The Airbus Concept Plane," https://airbus-h.assetsadobe2.com/is/image/content/dam/corporate-topics/innovation/future-concepts/concept-plane/Airbus-Concept_plane_-side_back_view_left.jpg?wid=991&fit=fit,1&qlt=85,0, 2010. Accessed: 2018-09-25.

[3] Allen, T. J., Sexton, B. W., and Scott, M. J., "SUGAR Truss Braced Wing Full Scale Aeroelastic Analysis and Dynamically Scaled Wind Tunnel Model Development," *56th AIAA/ASCE/AHS/ASC Structures, Structural Dynamics, and Materials Conference*, Kissimmee, Florida, 2015. doi:10.2514/6.2015-1171.

[4] Bradley, M. K., and Droney, C. K., "Subsonic Ultra Green Aircraft Research," *NASA/CR-2011-216847*, 2011.

[5] Wright, J. R., and Cooper, J. E., *Introduction to Aircraft Aeroelasticity and Loads*, Wiley, 2008.

[6] Géradin, M., and Cardona, A., *Flexible Multibody Dynamics - A Finite Element Approach*, Wiley, Chichester, England, U.K., 2001.

[7] Hesse, H., Palacios, R., and Murua, J., "Consistent Structural Linearization in Flexible Aircraft Dynamics with Large Rigid-Body Motion," American Institute of Aeronautics and Astronautics, 2014, pp. 528–538. doi:10.2514/1.J052316.

[8] Cesnik, C. E. S., and Brown, E. L., "Modeling of High Aspect Ratio Active Flexible Wings for Roll Control," *43rd AIAA/ASME/ASCE/AHS/ASC Structures, Structural Dynamics, and Materials Conference*, Denver, Colorado, 2002. doi:10.2514/6.2002-1719.

[9] Shearer, C. M., and Cesnik, C. E. S., "Nonlinear Flight Dynamics of Very Flexible Aircraft," *Journal of Aircraft*, Vol. 44, No. 5, 2007, pp. 1528–1545. doi:10.2514/1.27606.

[10] Su, W., and Cesnik, C. E. S., "Nonlinear Aeroelasticity of a Very Flexible Blended-Wing-Body Aircraft," *Journal of Aircraft*, Vol. 47, No. 5, 2010, pp. 1539–1553. doi:10.2514/1.47317.

[11] Hodges, D. H., "A Mixed Variational Formulation Based on Exact Intrinsic Equations or Dynamics of Moving Beams," *International Journal of Solids and Structures*, Vol. 26, No. 11, 1990, pp. 1253–1273. doi:10.1016/0020-7683(90)90060-9.

[12] Roger, K. L., "Airplane Math Modeling for Active Control Design," Proceedings of the 44th AGARD Structure and Materials Panel, 1977, pp. 4.1–4.11.

Review copy- Do not distribute

[13] Karpel, M., "Time Domain Aeroservoelastic Modeling Using Weighted Unsteady Aerodynamic Forces," *Journal of Guidance, Control and Dynamics*, Vol. 13, No. 1, 1990, pp. 30–37. doi:10.2514/3.20514.

[14] Patil, M. J., Hodges, D. H., and Cesnik, C. E. S., "Nonlinear Aeroelasticity and Flight Dynamics of High-Altitude Long-Endurance Aircraft," *Journal of Aircraft*, Vol. 38, No. 1, 2001, pp. 88–94. doi:10.2514/2.2738.

[15] Cook, R. G., Palacios, R., and Goulart, P., "Robust Gust Alleviation and Stabilization of Very flexible Aircraft," *AIAA Journal*, Vol. 51, No. 2, 2013, pp. 330–340. doi:10.2514/1.J051697.

[16] Peters, D. A., Karunamoorthy, S., and Cao, W., "Finite State Induced Flow Models. Part 1: Two-Dimensional Thin Airfoil," *Journal of Aircraft*, Vol. 32, No. 2, 1995, pp. 313–322. doi:10.2514/3.46718.

[17] Leishman, J. G., "Unsteady Lift of a Flapped Airfoil by Indicial Concepts," *Journal of Aircraft*, Vol. 31, No. 2, 1994, pp. 288–297. doi:10.2514/3.46486.

[18] Petot, D., "Differential Equation Modelling of Dynamic Stall," *La Reserche Aerospatiale*, , No. 5, 1989, pp. 59–71.

[19] Leishman, J. G., and Beddoes, T. S., "A generalized Model for Airfoil Unsteady Aerodynamic Behaviour and Dynamic Stall Using the Indicial Method," Proceedings of the 42nd Annual Forum of the American Helicopter Society, Washington D. C., 1986, pp. 528–538.

[20] Kier, T. M., "Comparison of Unsteady Aerodynamic Modelling Methodologies with respect to Flight Loads Analysis," *AIAA Atmospheric Flight Mechanics Conference and Exhibit*, San Francisco, California, 2005. doi:10.2514/6.2005-6027.

[21] Palacios, R., Murua, J., and Cook, R. G., "Structural and Aerodynamic Models in the Nonlinear Flight Dynamics of Very Flexible Aircraft," *AIAA Journal*, Vol. 48, No. 11, 2010, pp. 2648–2659. doi:10.2514/1.J050513.

[22] Wang, Z., Chen, P. C., Liu, D. D., and Mook, D. T., "Nonlinear Aeroelastic Analysis for A HALE Wing Including Effects of Gust and Flow Separation," 48th AIAA/ASME/ASCE/AHS/ASC Structures, Structural Dynamics, and Materials Conference, Honolulu, Hawaii, 2007. doi:10.2514/6.2007-2106.

[23] Murua, J., Hesse, H., Palacios, R., and Graham, J. M. R., "Stability and Open-Loop Dynamics of Very Flexible Aircraft Including Free-Wake Effects," 52nd AIAA/ASME/ASCE/AHS/ASC Structures, Structural Dynamics and Materials Conference, Denver, Colorado, 2011. doi:10.2514/6.2011-1915.

[24] Valente, C., Jones, D., Gaitonde, A., Cooper, J., and Lemmens, Y., "OpenFSI interface for strongly coupled steady and unsteady aeroelasticity," *International Forum on Aeroelasticity and Structural Dynamics, IFASD 2015*, International Forum on Aeroelasticity and Structural Dynamics (IFASD), 2015, pp. 591–606.

[25] Bekemeyer, P. and Ripepi, M. and Heinrich, R. and Görtz, S., "Nonlinear Unsteady Reduced Order Models based on Computational Fluid Dynamics for Gust Loads Predictions," *2018 Applied Aerodynamics Conference*, American Institute of Aeronautics and Astronautics Inc, AIAA, 2018. doi:10.2514/6.2018-3635.

For Peer Review

[26] Valente, C., Lemmens, Y., Wales, C., Jones, D., Gaitonde, A., and Cooper, J., "A Doublet-Lattice Method Correction Approach for High Fidelity Gust Loads Analysis," *58th AIAA/ASCE/AHS/ASC Structures, Structural Dynamics, and Materials Conference*, American Institute of Aeronautics and Astronautics Inc, AIAA, 2017. doi:10.2514/6.2017-0632.

[27] Horwitz, R. A. D., Liw Tat Man, W., Malan, A. G., and Braithwaite, J., "A Kriging Based Corrected Potential Flow ROM for Gust Load Calculations," *2018 Applied Aerodynamics Conference*, American Institute of Aeronautics and Astronautics Inc, AIAA, 2018. doi:10.2514/6.2018-3633.

[28] Calderon, D. E., Cooper, J. E., Lowenberg, M. H., Neild, S., and Coetzee, E., "Sizing High-Aspect-Ratio Wings with a Geometrically Nonlinear Beam Model," *Journal of Aircraft (Article in Advance)*, 2019. doi:10.2514/1.C035296.

[29] Calderon, D. E., Cooper, J. E., Lowenberg, M. H., Neild, S., and Coetzee, E., "On the Effect of Including Geometric Nonlinearity in the Sizing of a Wing," *SciTech 2018*, Kissimmee, Florida, 2018. doi:10.2514/6.2018-1680.

[30] Howcroft, H., Cook, R. G., Calderon, D. E., Lambert, L. A., Castellani, M., Cooper, J. E., Lowenberg, M. H., Neild, S. A., and Coetzee, E. B., "Aeroelastic Modelling of Highly Flexible Wings," *57th AIAA/ASCE/AHS/ASC Structures, Structural Dynamics, and Materials Conference*, San Diego, California, 2016. doi:10.2514/6.2016-1798.

[31] Jones, W. P., "Aerodynamic Forces on Wings in Non-uniform Motion," *ARCR & M 2117*, 1945.

[32] Shearer, C. M., and Cesnik, C. E. S., "Modified Generalized-α Method for Integrating Governing Equations of Very Flexible Aircraft," *47th AIAA/ASME/ASCE/AHS/ASC Structures, Structural Dynamics, and Materials Conference*, Newport, Rhode Island, 2006. doi:10.2514/6.2006-1747.

[33] "FAA Federal Aviation Regulations, Section 25.341," `http://www.flightsimaviation.com/data/FARS/part_25-341.html`, 2018. Accessed: 2018-09-25.

[34] European Aviation Safety Agency (EASA), *CS-25 Certification Specifications for Large Aeroplanes*, 2003.

[35] Cook, R. G., Wales, C. J. A., Gaitonde, A. L., Jones, D. P., and Cooper, J. E., "Uncertainty Quantification In Gust Loads Analysis Of a Highly Flexible Aircraft Wing," *International Forum on Aeroelasticity and Structural Dynamics*, Como, Italy, 2018.

[36] Cook, R. G., Wales, C. J. A., Gaitonde, A. L., Jones, D. P., and Cooper, J. E., "Efficient Modelling of a Nonlinear Gust Loads Process for Uncertainty Quantification of Highly Flexible Aircraft," *SciTech 2018*, Kissimmee, Florida, 2018. doi:10.2514/6.2018-1681.

[37] Allemang, R. J., "The modal assurance criterion–twenty years of use and abuse," *Sound and vibration*, Vol. 37, No. 8, 2003, pp. 14–23. doi:10.1016/j.proeng.2012.09.551.

[38] Hodges, D. H., Shang, X., and Cesnik, C. E. S., "Finite Element Solution of Nonlinear Intrinsic Equations for Curved Composite Beams," *Journal of the American Helicopter Society*, Vol. 41, No. 9, 1996. doi:10.2514/6.1995-1174.

For Peer Review